SANDIA REPORT

SAND2015-1316
Unlimited Release
Printed December 2014

Correcting Cross-polarization Monopulse Response of Reflector Antennas

Billy C. Brock and Steven E. Allen

Prepared by
Sandia National Laboratories
Albuquerque, New Mexico 87185 and Livermore, California 94550

Sandia National Laboratories is a multi-program laboratory managed and operated by Sandia Corporation, a wholly owned subsidiary of Lockheed Martin Corporation, for the U.S. Department of Energy's National Nuclear Security Administration under contract DE-AC04-94AL85000.

Issued by Sandia National Laboratories, operated for the United States Department of Energy by Sandia Corporation.

Available to DOE and DOE contractors from

U.S. Department of Energy
Office of Scientific and Technical Information
P.O. Box 62
Oak Ridge, TN 37831

Telephone: (865) 576-8401
Facsimile: (865) 576-5728
E-Mail: reports@adonis.osti.gov
Online ordering: http://www.osti.gov/bridge

Available to the public from

U.S. Department of Commerce
National Technical Information Service
5285 Port Royal Rd.
Springfield, VA 22161

Telephone: (800) 553-6847
Facsimile: (703) 605-6900
E-Mail: orders@ntis.fedworld.gov
Online order: http://www.ntis.gov/help/ordermethods.asp?loc=7-4-0#online

SAND2015-1316
Unlimited Release
Printed December 2014

Correcting Cross-polarization Monopulse Response of Reflector Antennas

Billy C. Brock and Steven E. Allen
ISR EM and Sensor Technologies
Sandia National Laboratories
P.O. Box 5800
Albuquerque, New Mexico 87185-0533

Abstract

The monopulse response of radar systems utilizing a short-focal-length offset-fed parabolic reflector can be compromised by depolarization of the signal by the target and by multipath scattering from nearby objects. The polarimetric behavior of this type of antenna is examined. The use of a shroud to reduce multipath interaction with nearby objects is also described. The mechanism through which man-made targets can introduce cross-polarization components into the scattered field is explained. Two kinds of polarization filters, suitable for linear polarization, are described for mitigating the effects of depolarization due to cross-polarization scattering. The benefit of the application of a polarization filter is demonstrated by modeling a monopulse radar system viewing a dihedral corner reflector. The model demonstrates dramatic performance improvement when the filter is used, showing that usable performance can be achieved even when the target depolarization is so severe that the cross-polarized signal is more than an order of magnitude stronger than the desired co-polarized signal. Relevant and useful reference material is also included in the form of appendices describing the relationship between different polarization representations and demonstrating the conditions under which Maxwell's equations can be considered to be scale-invariant.

Acknowledgements

This report is the result of a Cooperative Research and Development Agreement (CRADA) between Sandia National Laboratories and General Atomics Aeronautical Systems, Inc. – CRADA No. SC08/01749.

Sandia National Laboratories is a multi-program laboratory managed and operated by Sandia Corporation, a wholly owned subsidiary of Lockheed Martin Corporation, for the U.S. Department of Energy's National Nuclear Security Administration under contract DE-AC04-94AL85000.

General Atomics Aeronautical Systems, Inc. (GA-ASI), an affiliate of privately-held General Atomics, is a leading manufacturer of Remotely Piloted Aircraft (RPA) systems, radars, and electro-optic and related mission systems, including the Predator®/Gray Eagle®-series and Lynx® Multi-mode Radar.

Contents

Foreword

This report details the results of an academic study. It does not presently exemplify any operational systems with respect to modes, methodologies, or techniques.

Classification

The specific mathematics and algorithms presented herein do not bear any release restrictions or distribution limitations.

The distribution limitations of this report are in accordance with the classification guidance detailed in the memorandum "Classification Guidance Recommendations for Sandia Radar Testbed Research and Development", DRAFT memorandum from Brett Remund (Deputy Director, RF Remote Sensing Systems, Electronic Systems Center) to Randy Bell (US Department of Energy, NA-22), February 23, 2004. Sandia has adopted this guidance where otherwise none has been given.

This report formalizes preexisting informal notes and other documentation on the subject matter herein.

Introduction

A monopulse tracking radar uses special features of the antenna to obtain an accurate estimate of the direction to a target, using only a single transmitted pulse [1]. Although both amplitude-comparison and phase-comparison schemes exist, it is the amplitude-comparison scheme that is most compatible with a single reflector antenna. This system utilizes an antenna with multiple overlapping beams, clustered symmetrically about a boresight direction, to estimate the angular distance from the boresight direction to the target. A single-axis monopulse system will use two overlapping beams, while a dual-axis system will typically use four overlapping beams. In the single-axis system, the two beams are added to produce a sum pattern and subtracted to produce a difference pattern. For the dual-axis system, all four beams are added to produce the sum pattern, while differences between sums of pairs of beams are formed to produce two orthogonal difference patterns. The radar transmits a single pulse through the sum pattern, illuminating the target. The return signal from the target is received through both the sum and difference patterns. By comparing the response from the difference patterns to that of the sum pattern, the direction to the target can be estimated accurately to within a fraction of the beam width of the sum pattern.

The accuracy of a monopulse tracker can be degraded by extraneous signals entering the radar receiver through the difference patterns. Two common sources of extraneous signals are multi-path reflections from nearby objects and the less-than-ideal polarization[1] response of the antenna itself. As the title suggests, the current focus will be on mitigating the poor cross-polarization response of the antenna. However, controlling the response to multi-path reflections is also important, and will be addressed briefly.

For simplicity, the performance of a single-axis monopulse antenna will be examined. Through extension, this material also applies directly to the dual-axis monopulse system. The monopulse radiation pattern will be obtained from an offset-fed reflector antenna, which will be described in the first section. Next, the depolarization mechanism through which cross-polarized signals are generated by scattering from man-made objects is described. Then, the issue of controlling the response arising from multi-path interactions with nearby objects is briefly discussed. Finally, mitigating the cross-polarization response through the use of a polarization filter is described and demonstrated. Design equations are included for determining the geometrical dimensions of the filter that are required to achieve specified performance.

Because of the importance of polarization, Appendix I describes several sets of basis vectors used to describe polarization, and the relationship between the sets. Scale invariance of Maxwell's equations is important for the validity of the design equations presented, so Appendix II examines the conditions necessary for scale invariance to apply to Maxwell's equations.

Polarization response of an offset-fed reflector antenna

The geometry of a parabolic reflector antenna causes it to radiate some amount of the cross-polarization component, even when the feed radiates a pure polarization. The phenomenon is well known, and is exaggerated when the ratio of the focal length to the diameter, F/D, is small [3, 4, 5]. Because of space limitations, when reflector antennas are used in airborne applications, they typically will have small values for F/D. Although the cross-polarization response for symmetric reflectors can be very low in the direction of the boresight, that is not the case for offset-fed reflectors, which can exhibit high levels of

[1] Polarization refers to the direction of the electric-field vector, which can be constant with time (linear polarization) or rotate with time (elliptical polarization). The principal or primary polarization will be referred to as the co-polarization component, and the orthogonal polarization will be referred to as the cross-polarization component. While polarization refers to the direction of the electric-field vector in the subjects of radar, microwaves, and RF, in the older subject of optics, for historical reasons, it usually refers to the direction of the magnetic-field vector [2].

cross polarization [6]. Thus, offset-fed reflectors with small F/D will radiate and receive a significant amount of the cross-polarized field. This will be demonstrated with the following example.

Consider the offset-fed reflector illustrated for several viewing positions in Figure 1. The reflector is cut from a paraboloid with a focal length of 150 mm, and has an elliptical silhouette. The width of the reflector is 600 mm and the height is 300 mm. To reduce the aperture blockage from the feed structure (not shown), the base of the reflector is offset from the origin along $\hat{\mathbf{y}}$ by 50 mm. The focal point, which lies on the $\hat{\mathbf{z}}$ axis, is shown with a red dot in Figure 1. Using the major diameter of the reflector, the F/D ratio is 0.25, putting it in the class of short-focal-length reflectors.

The polarization performance for this reflector will be demonstrated with computed radiation patterns, produced when it is fed with a pair of open-ended circular waveguides representing the monopulse feed. The two feeds will be placed in the focal plane, but symmetrically offset slightly from the focal point along the $\hat{\mathbf{x}}$ direction. The pair of feeds produces two overlapping beams, squinted slightly to opposite sides of the boresight direction. Exciting the feeds with the same phase will produce the sum pattern, aligned with the boresight, while providing a $180°$ phase offset between the feeds will produce the difference pattern needed by the monopulse radar. Thus, this example will be appropriate for a single-axis monopulse system. No effort has been made to optimize the reflector and feed for any specific purpose, but it is intended to be representative and to demonstrate the principles that are involved.

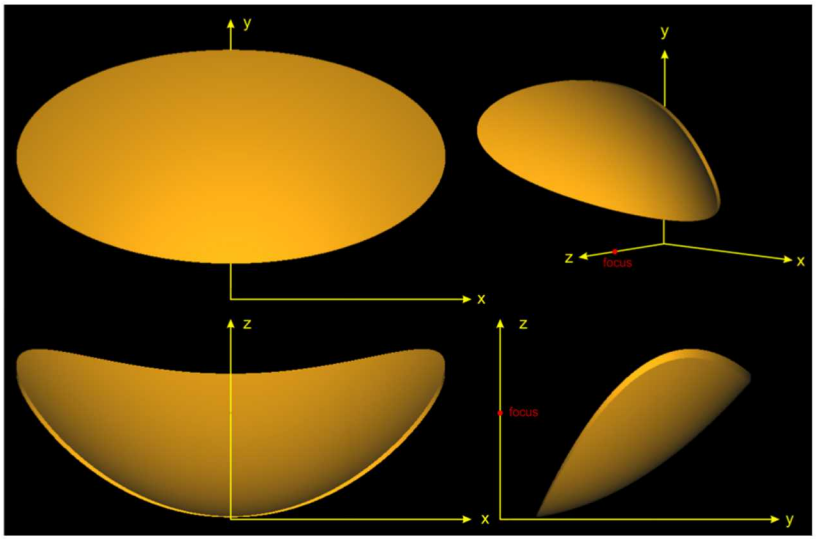

Figure 1 *Illustration of the short-focal-length off-set-fed reflector that is used to illustrate the polarization issues.*

In this example, the feeds will be vertically polarized, with the electric field oriented in the $\hat{\mathbf{y}}$ direction. The open-ended circular waveguides provide a suitably tapered illumination, producing low side lobes. The side lobes contained in the principal plane normal to $\hat{\mathbf{x}}$ will be the highest. This is a consequence of the narrow height of the reflector and the fact that the feed's radiation pattern is stronger in the direction of the narrow-dimension edge. The fully polarimetric radiation patterns for the feeds used in this analysis were computed with the time-domain solver in *CST Microwave Studio*® [7]. The radiation patterns produced by the reflector were computed with the *AntFarm*™ software [8], which uses physical-optics currents on the reflector resulting from the previously computed feed radiation pattern.

The partial-gain radiation patterns[2] are displayed using the linear Ludwig 3 polarization components, with V polarization aligned with the y-axis in Figure 1. The H polarization is aligned with the x-axis. The radiation patterns will be displayed with standard spherical coordinates, as shown in Figure 2. The Ludwig 3 polarization basis is very useful for describing the radiation from a high-gain antenna, although there are a number of different basis sets that can be used, with some more suitable than others for a specific purpose. It is quite common to call V and H polarization vertical and horizontal, respectively. However, since these polarization directions are directly tied to a coordinate system attached to the antenna, and since the antenna can be tilted and rotated to any arbitrary position, the polarization basis may not correspond to the *local* vertical and horizontal directions defined by the local zenith and horizon. See Appendix I for a detailed description of the Ludwig 3 (L3) polarization basis vectors and their relation to other common polarization basis vectors.

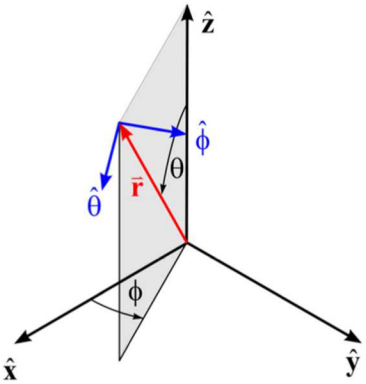

Figure 2 *The standard right-handed spherical coordinate system, showing the angles* (θ,ϕ) *locating the field point and the spherical polarization basis vectors,* $\hat{\theta}$ *and* $\hat{\phi}$*, at the field point.*

For this example, the V polarization is the primary polarization (also called co-polarization) and H is the cross-polarization. The portion of the sum-channel radiation pattern near the center of the main beam is displayed in Figure 3, with the primary (V) polarization pattern on the left and the cross-polarization (H) on the right. The angle ϕ is plotted around the periphery of the polar plot, with θ measured along the radius from the center. The coordinates $\phi = 0°$ and $\phi = 90°$ are respectively aligned with the x and y axes illustrated in Figure 1. In Figure 3, the increment between the concentric rings is $\Delta\theta = 2.5°$, so the plot covers the forward region defined by $0° \le \theta \le 15°$. The side lobes are highest near the y-z plane, with the peak side lobe about 16 dB down. However, the side lobes near the x-z plane are low enough not to be visible in this plot. In the y-z plane, the cross-polarization level is very low, but outside of the y-z plane in the region of the main lobe of the sum pattern, the cross-polarization is significant, down only about 15 dB from the boresight peak.

The difference pattern is plotted in Figure 4, with $\Delta\theta = 2.5°$, and with a magnified view in Figure 5, where $\Delta\theta = 0.5°$. For the primary polarization (on the left), the monopulse null is very well defined and quite narrow, which should allow very good single-axis direction resolution with the monopulse radar. However, the cross-polarization pattern is quite high in the boresight direction near the y-z plane, and is only about 7 dB down from the principal polarization peak. When the target exhibits significant cross-polarization response, this antenna will not produce a very good monopulse response. Since the cross-polarization response of the target cannot be controlled, it will be necessary to modify the cross-polarization response of the antenna to achieve adequate performance.

[2] Partial gain is the gain associated with a *single* polarization component, while total gain considers the contributions from both orthogonal polarization components.

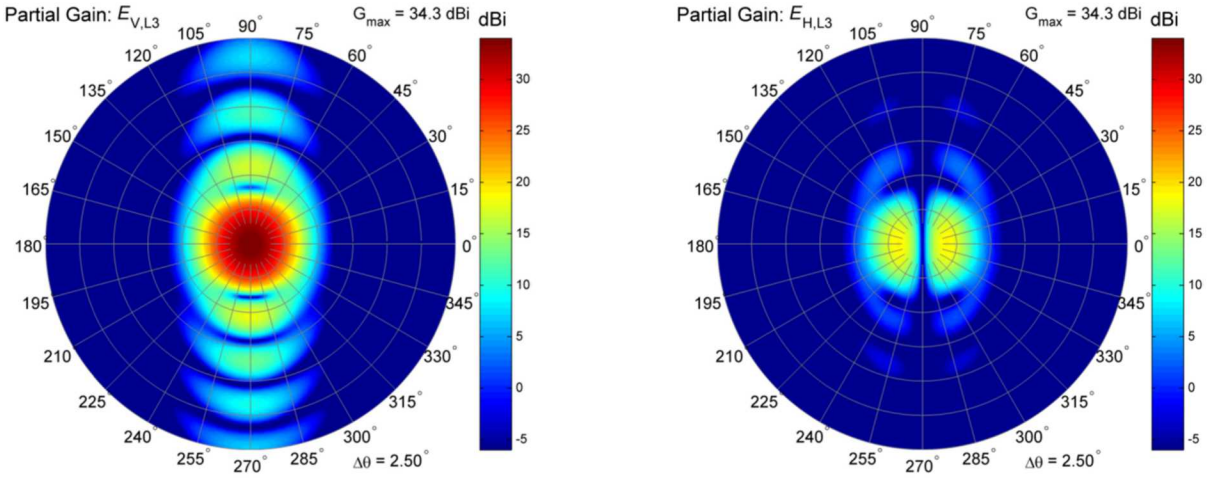

Figure 3 *Sum-channel radiation patterns near the bore-sight direction for the offset-fed reflector in Figure 1 (Ludwig 3 linear polarizations).*

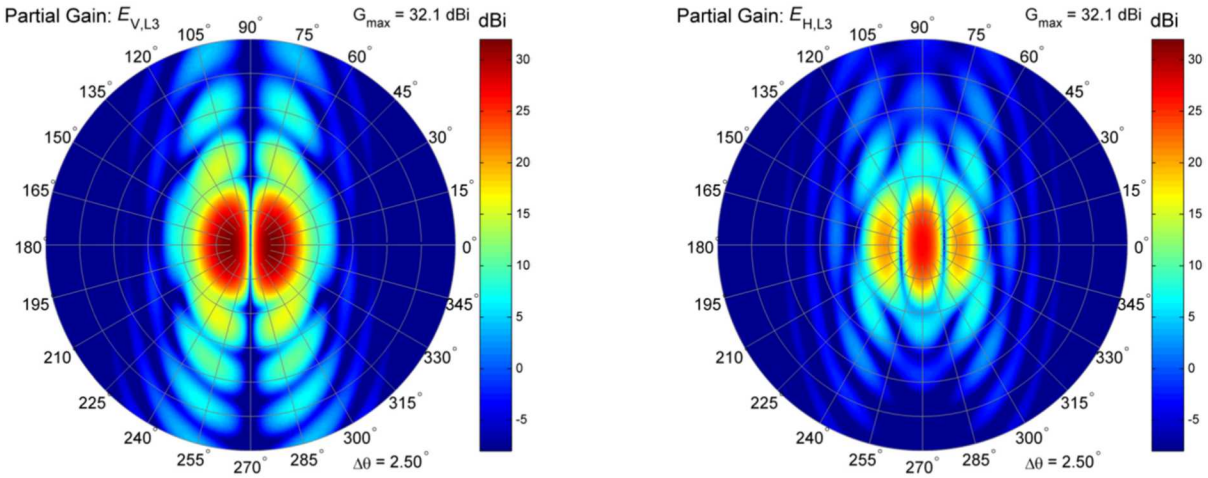

Figure 4 *Difference-channel radiation patterns near the bore-sight direction for the offset-fed reflector in Figure 1 (Ludwig 3 linear polarizations).*

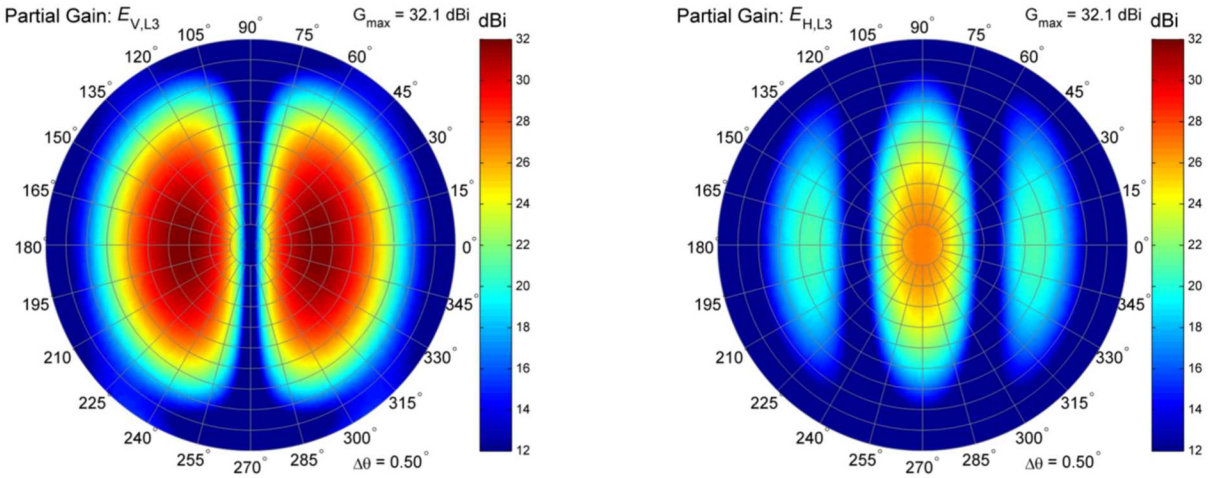

Figure 5 *Close-up look at the difference-channel radiation patterns near the bore-sight direction for the offset-fed reflector in Figure 1 (Ludwig 3 linear polarizations).*

Polarization rotation upon reflection from man-made objects

Many man-made objects incorporate flat surfaces or surfaces with large radius of curvature, which are attached along edges to other similar surfaces. These dihedral-like structures can support multiple reflections of the radar signal, and when the surface-normal vectors are neither parallel nor perpendicular to the electric-field vectors, the reflections can rotate the electric-field vector. Thus, the polarization of the signal scattered from many objects of interest can be different from that of the incident signal. Since the difference pattern of a short-focal-length reflector can exhibit significant cross-polarization response in the region of the monopulse null, polarization rotation by the target can detrimentally impact position estimates obtained from the monopulse radar mode.

Consider the simple dihedral illustrated in Figure 6, where the two flat plates are perpendicular. On the left, unit vectors for vertical and horizontal electric fields are depicted as incident upon a dihedral where the corner seam is aligned with the vertical unit vector. On the right, the corner seam is rotated by an angle α from the vertical direction toward the horizontal direction. The important features of the dihedral can be determined with analysis based on physical optics [9, 10], while more subtle features require more detailed analysis [11, 12, 13].

It is instructive to examine the left side of Figure 6, applying boundary conditions for a perfect electric conductor for the plates of the dihedral. Since the vertical unit vector lies in the plane of the dihedral plates, the scattering of the vertical electric field is relatively easy to visualize. When the vertical incident field encounters the plate, the scattered electric-field vector direction changes by 180° so that the total electric field on the surface is zero. It then propagates across to the other plate, and upon reflection, it changes direction again by 180°. The net effect is no change in the reference direction of the vertical component of the electric field.

The visualization of the behavior of the horizontal component of the electric field is a bit more complicated because the horizontal unit vector does not lie in the plane of dihedral plates. The horizontal unit vector must be decomposed into a component in the plane of the plate, and a component normal to the plate. With the geometry on the left of Figure 6, the components have equal length, $1/\sqrt{2}$. Since the total electric field tangential to the plate must be zero, the reflected component parallel to the plate must be rotated by 180°. However, the component normal to the plate is not changed. This makes the scattered electric field vector rotate by 90° as illustrated. Upon reaching the other plate, the same process occurs, rotating the scattered electric-field vector by another 90°, in the same direction. The result is that the scattered horizontal component of the electric field changes direction by 180°.

The fact that the vertical component of the electric field does not change direction upon reflection from the dihedral, while the horizontal component does, gives the dihedral its polarization-altering property. When the vertical and horizontal components of the electric field are incident on the dihedral on the right side of Figure 6, the complex scattering matrix behaves according to

$$\gamma = \begin{bmatrix} \gamma_{h,h} & \gamma_{h,v} \\ \gamma_{v,h} & \gamma_{v,v} \end{bmatrix} = \gamma_{dihedral} \begin{bmatrix} -\cos 2\alpha & \sin 2\alpha \\ \sin 2\alpha & \cos 2\alpha \end{bmatrix}, \tag{1}$$

where the second subscript represents the direction of the incident electric field, and the first subscript describes the direction of the scattered electric field. The components, $\gamma_{i,j}$, of the complex scattering matrix are complex lengths, carrying the phase of the electric field, and the traditional radar-cross-section (RCS) scattering matrix is given by

$$\sigma = \begin{bmatrix} \sigma_{h,h} & \sigma_{h,v} \\ \sigma_{v,h} & \sigma_{v,v} \end{bmatrix} = \begin{bmatrix} |\gamma_{h,h}|^2 & |\gamma_{h,v}|^2 \\ |\gamma_{v,h}|^2 & |\gamma_{v,v}|^2 \end{bmatrix}, \tag{2}$$

where the components, $\sigma_{i,j}$, are areas representing the radar cross section when viewed with the i^{th} incident polarization and the j^{th} scattered polarization. When $\alpha = 22\frac{1}{2}°$, an incident signal of either pure vertical or pure horizontal polarization will scatter equal amounts of both polarizations. However, when $\alpha = 45°$, the incident pure vertical or pure horizontal polarization will be transformed upon scattering into pure horizontal or pure vertical polarization, respectively. The ratio of the cross-polarized to the co-polarized RCS is plotted in Figure 7 as a function of the rotation angle, α. It is this behavior of the dihedral that causes many man-made objects such as aircraft, trucks, and other vehicles to scatter significant amounts of cross polarization when illuminated by radar.

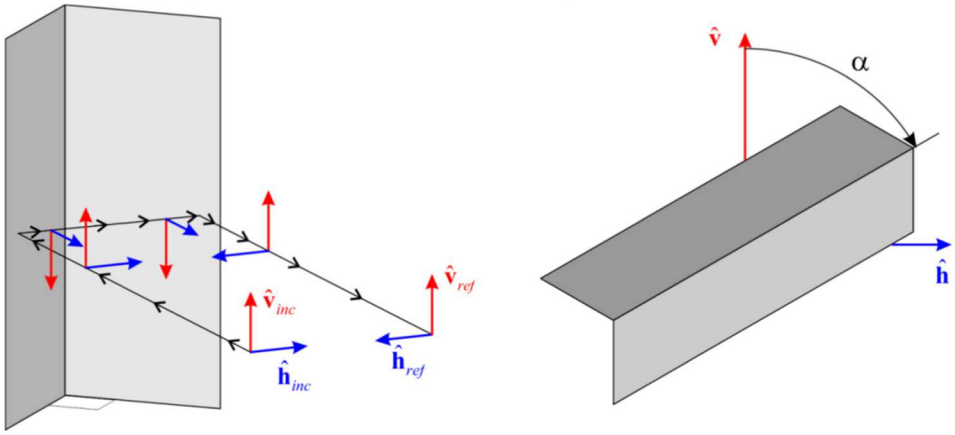

Figure 6 *Illustration of electric-field unit-vector directions for normal-incidence first-order scattering from a dihedral. The vertically polarized electric field is parallel to the vertex seam, while the horizontally component is perpendicular to the seam.*

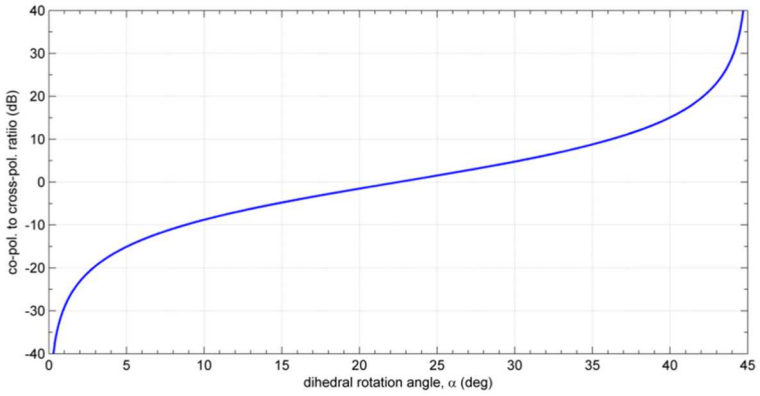

Figure 7 *Ratio of the cross-polarized to co-polarized RCS for the dihedral for* $0 \le \alpha \le 45°$.

Use of an antenna shroud to reduce interaction with aircraft

When the antenna is mounted on a structure such as an aircraft, there are many nearby surfaces and edges that can produce reflection and diffraction that directs energy toward the side lobes of the antenna's radiation pattern. This applies not just to the radiation pattern of the reflector, but also to radiation pattern of the feed itself. Depending on how the reflector and feed are oriented, the spill-over from the feed will

also illuminate the surfaces of various parts of the aircraft. In addition, as described above, these surfaces and edges can cause rotation of the electric-field vector, changing the polarization.

Obviously, reflections from various surfaces on the aircraft can interfere with the intended response of the difference pattern required for monopulse operation. Regardless of whether or not these reflections are polarized in the primary or cross-polarization direction, they will compete with the desired signal response of the monopulse pattern, potentially filling in the central null. The undesirable multi-path interaction can be significantly reduced through the application of a shroud around the antenna, its feed, and other structures near the antenna, as described in U.S. Patent 6661368 [14].

The purpose of the shroud is to simply block the radiation arriving at the antenna from directions other than near the boresight. Figure 8 illustrates a dual-phase-center gimbaled reflector antenna mounted on a model of a representative unmanned aircraft system. The antenna is mounted near the front of the aircraft, with the shroud depicted in green. The wings, body, stabilizer, and propeller can all contribute reflections that can enter the unshrouded antenna; depending, of course, on the direction the antenna is pointed on its gimbal.

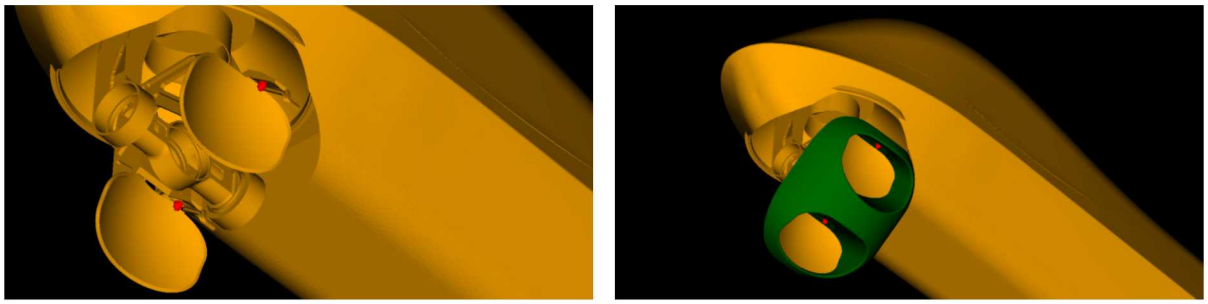

Figure 8 *Illustration of a dual-phase-center antenna mounted on a model of a representative unmanned aircraft. The antenna is shown with and without the shroud (green) that is designed to minimize the antenna interaction with reflections from the aircraft. (The red spots near the upper middle of the parabolic reflectors represent the location of the feed horn, which is not shown.)*

Although analysis with geometric optics ignores contributions due to diffraction from the edges of the shroud, ray tracing is a very effective method of visualizing the benefit obtained from applying the shroud. Figure 9 shows the ray paths resulting from excitation of the upper reflector of the pair, without the presence of the shroud. The blue lines represent the paths of rays that reflect only once (from the reflector), while the other colors represent ray paths that include multiple reflections. The direct rays from the feed are not shown. Many of the multiple reflections occur near the antenna, reflecting from the portions of the fuselage that are close to the antenna. However, even with the antenna in the orientation indicated, there are some rays that enter the antenna after reflecting from the under-surface of the wing. In this example, the location of the antenna near the front of the body, combined with pointing the antenna to the side, limits the number of rays reflecting directly from the wings. That will not always be case when the antenna is squinted away from broadside.

Figure 10 illustrates the result of ray-trace analysis after the shroud is attached to the antenna. The vast majority of the multipath rays have been eliminated, and the ray tracing shows mostly the desired collimated radiation from the antenna. It appears that the remaining rays reflecting from the body and the wing are actually coming from the region just above the shroud, indicating that minor adjustments to the shape in this area could be effective in eliminating the remaining multipath contributions. Although the primary purpose of the shroud is to block energy reflecting from the surfaces of the aircraft, multiple reflections can occur between the shroud structure and other surfaces, so treating it with microwave absorber can improve its performance.

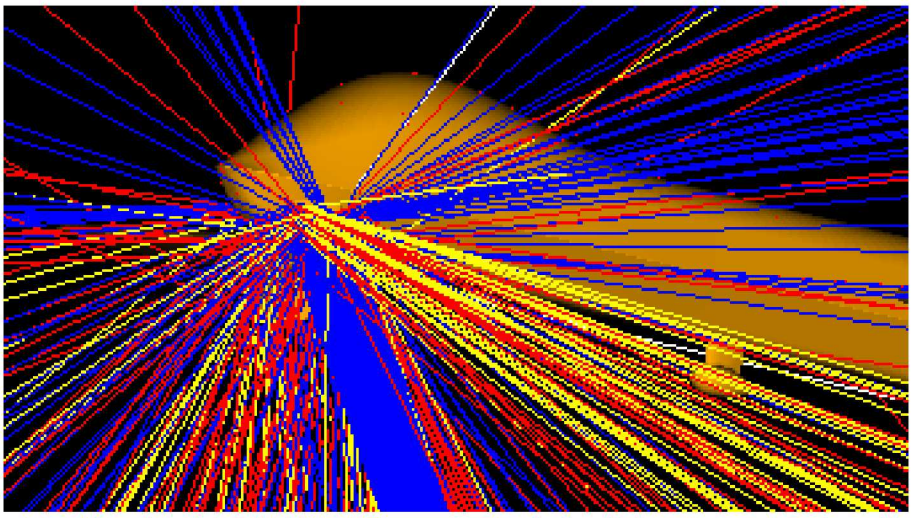

Figure 9 *Ray-trace illustration of the interaction of the unshrouded antenna (top reflector) with the aircraft. The blue rays correspond to one reflection (from the antenna reflector or some other structure), while the other colors represent multiple reflections.*

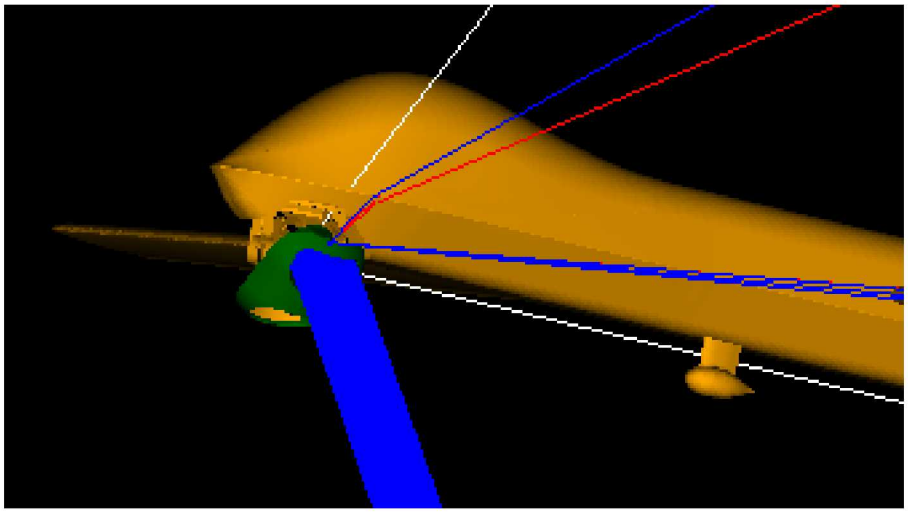

Figure 10 *Ray-trace illustration of the interaction of the shrouded antenna (top reflector) with the aircraft. The meaning of the ray colors matches that of Figure 9. The effect of the shroud is to greatly reduce the interaction with the aircraft body.*

Diffraction will occur at the edge of the shroud, and does have the potential to adversely affect performance. However, using appropriate microwave absorber on the surfaces of the shroud, including the interior, can reduce the currents on those surfaces, and thus reduce the level of diffraction that occurs at the edge discontinuities. Careful shaping of the shroud can also be useful in controlling reflections directly from it and in controlling where the edge diffraction components go. Here, analysis using the principals of the geometrical theory of diffraction [15] or uniform geometrical diffraction theory [16, 17], through tracing the diffraction cones, can be useful. The shroud should also be designed with consideration for the illumination taper in the antenna near-field region to minimize any impact on the far-field radiation pattern.

Polarization filter

A polarization filter is designed to pass a specified polarization, as defined by the direction of the electric-field vector, while rejecting the orthogonal polarization. Wide-bandwidth filters can be designed for linear polarization by placing an appropriately spaced set of linear conductors (for example wires) parallel to the electric-field vector to be rejected. By adjusting the spacing and size of the conductors, the amount of rejection can be controlled. For the electric-field component orthogonal to the axis of the conductors there will be efficient transmission, although with some small amount of insertion loss. Though typically small, the insertion loss for the desired polarization will increase as the width of the conductor becomes a larger fraction of the spacing between conductors. Two implementations of the polarization filter will be examined:

1) the wire-grid filter, with copper wires suspended in air, and
2) the circuit-trace filter, with copper circuit traces on a thin substrate of Rogers RT/duroid® 5880.

Insight into the operation of the polarization filter can be obtained by considering the boundary conditions on the electric field at the linear conductors and applying the equivalence principle of electromagnetics. The boundary conditions require the tangential electric field to be near zero on the conductor (exactly zero for a perfect electric conductor, PEC). This causes currents to flow on the conductor surface that produce an electric field opposing the incident field. For the electric-field component parallel to the linear conductor, this current is significant. However, for the component perpendicular to the linear conductor, the current is quite small. According to the surface equivalence principle of electromagnetics [18], the scattered field is that obtained by removing all of the conductors and replacing them with the surface currents. The total field is obtained by adding the incident field to the scattered field. In the forward direction, the scattered field tends to cancel the incident field component having the same electric-field direction. Since the current induced by the component parallel to the conductor is much larger than that induced by the perpendicular component, its effect is much more significant. The end result is that the electric-field component parallel to the linear conductors is significantly attenuated upon passing through the structure, while the perpendicular component is only slightly affected.

An analytic theory for the behavior of the polarization filter is not included here. Instead, simulations have been performed over a fixed frequency band for a variety of dimensions defining the polarization filters. The entire structure for each type of filter can be described with just two or three dimensions:

wire-grid filter $\Rightarrow$ wire radius, r, and center-to-center wire spacing, δ.

circuit-trace filter $\Rightarrow$ trace width, w, center-to-center trace spacing, δ, and dielectric thickness, t.

To determine the effectiveness of the polarization rejection, the two filter types were modeled with the transient (time-domain) solver in *CST Microwave Studio*® [7]. The wire-grid filter model is illustrated in Figure 11a, while the circuit-trace filter is illustrated in Figure 11b. The simulations are excited by a plane wave incident upon a planar array of either PEC wires or PEC circuit traces that are oriented along the $\hat{\mathbf{x}}$ direction. The plane wave is incident along the $\hat{\mathbf{z}}$ direction. The Cartesian coordinate system with axes $\hat{\mathbf{x}}, \hat{\mathbf{y}}, \hat{\mathbf{z}}$ can be seen in Figure 11. Each planar grid is arranged in a cell with periodic boundary conditions, intended to simulate an infinite array. The faces of the bounding box normal to $\hat{\mathbf{x}}$ represent one pair of periodic boundaries, and the faces normal to $\hat{\mathbf{y}}$ represent the other pair. The faces normal to $\hat{\mathbf{z}}$ are open boundaries, with the incident plane wave propagating in the $+\hat{\mathbf{z}}$ direction. The cross-polarization rejection is defined by the ratio of the field strength of the $\hat{\mathbf{x}}$ component of the electric field after passing through the grid to that of the $\hat{\mathbf{x}}$ component of incident plane wave. The co-polarization insertion loss is defined similarly for the $\hat{\mathbf{y}}$ component of the electric field.

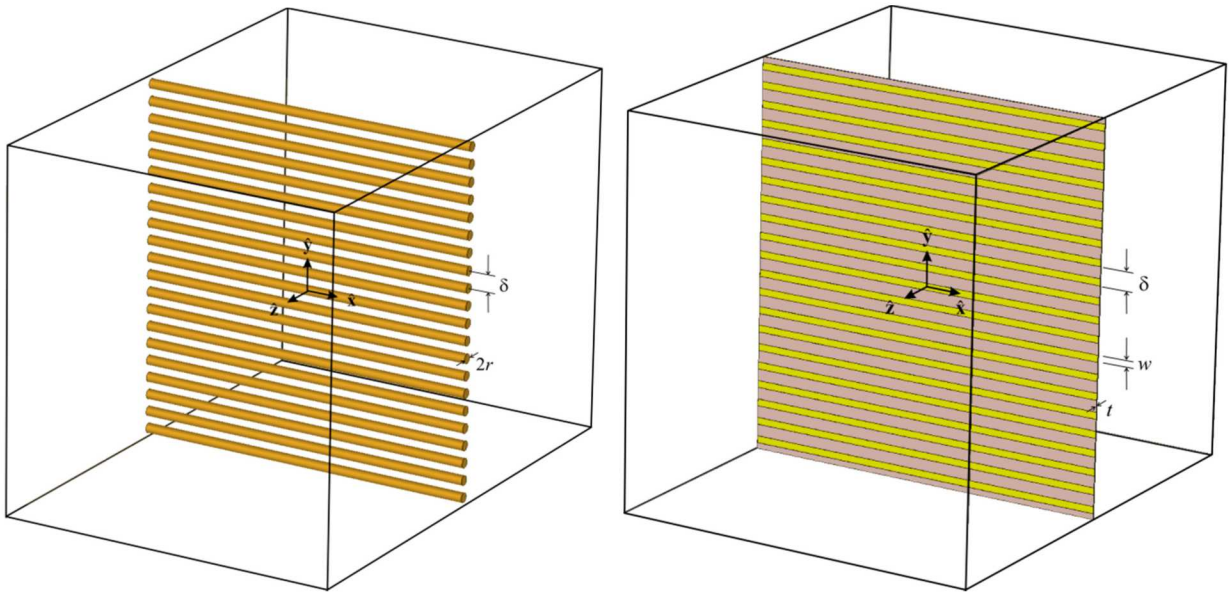

(a) (b)

Figure 11 *Wire-grid (left) and circuit-trace (right) models of the polarization filet, placed in the periodic cell, as modeled in CST Microwave Studio®.*

Because of the scale-invariance of Maxwell's equations, the data from specific simulations can be generalized by normalizing the defining dimensions by the wavelength, λ. The computed data can thus be applied accordingly to a wide range of frequencies. See Appendix II for more information about the specific conditions that allow scale-invariance of Maxwell's equations.

The polarization rejection of the wire-grid filter is determined by the wire radius, r, the wire spacing, δ, and the wavelength of the signal, λ. The generalized rational approximation to the polarization-rejection values (in decibels) predicted by simulations in *CST Microwave Studio* is

$$T_{\text{cross-pol}} = \frac{-\frac{286}{5}\left(1+\frac{362}{3}\left(1-\frac{119}{10}\left(1-\frac{238}{13}\left(1-\frac{93}{22}\frac{r}{\lambda}\right)\frac{r}{\lambda}\right)\frac{r}{\lambda}\right)\frac{r}{\lambda}-\frac{80}{23}\frac{\delta}{\lambda}\right)}{1-\frac{443}{4}\left(1-\frac{35}{3}\left(1-\frac{185}{31}\frac{r}{\lambda}\right)\frac{r}{\lambda}\right)\frac{r}{\lambda}+\frac{426}{7}\left(1-\frac{28}{15}\left(1-\frac{69}{20}\frac{\delta}{\lambda}\right)\frac{\delta}{\lambda}\right)\frac{\delta}{\lambda}}. \tag{3}$$

The data from which this approximation was computed comprise 63 different combinations of wire radius and spacing, spanning the non-normalized values $1.0 \le \delta \le 6.0$ mm, and $0.03125 \le r \le 1.75$ mm, over the frequency band $15.2 \le f \le 18.2$ GHz. This data is plotted in Figure 12, along with the approximation (3) for several values of r from the range given above. Agreement is sufficient for design purposes.

The rational approximation for the transmission coefficient, in decibels, for the co-polarization component is

$$T_{\text{co-pol}} = \frac{\frac{-20}{291}\left(1-\frac{2,391}{8}\left(1-\frac{78}{19}\left(1+427\frac{r}{\lambda}\right)\frac{r}{\lambda}\right)\frac{r}{\lambda}+\frac{907}{19}\frac{\delta}{\lambda}\right)}{1-\frac{1,754}{9}\left(1-\frac{883}{37}\left(1-\frac{269}{18}\left(1-\frac{255}{52}\frac{r}{\lambda}\right)\frac{r}{\lambda}\right)\frac{r}{\lambda}\right)\frac{r}{\lambda}+\frac{1,206}{41}\left(1+\frac{68}{25}\left(1+\frac{87}{68}\frac{\delta}{\lambda}\right)\frac{\delta}{\lambda}\right)\frac{\delta}{\lambda}}. \tag{4}$$

The values computed with *CST Microwave Studio*, along with the values obtained from (4), are plotted in Figure 13. Note that the formulas for the transmission coefficients are logarithmic (decibel) values.

The nature of rational approximations is such that poles exist for some values of the parameters, which are in general complex and may not necessarily be realized when the parameters are constrained to be real valued, as is the case here. However, approaching the poles too closely can cause the approximation to give unrealistic results. The parameters must be limited in range. The recommended space of r/λ and δ/λ for which (3) and (4) give valid and useful results is shown in Figure 14 and Figure 15, respectively.

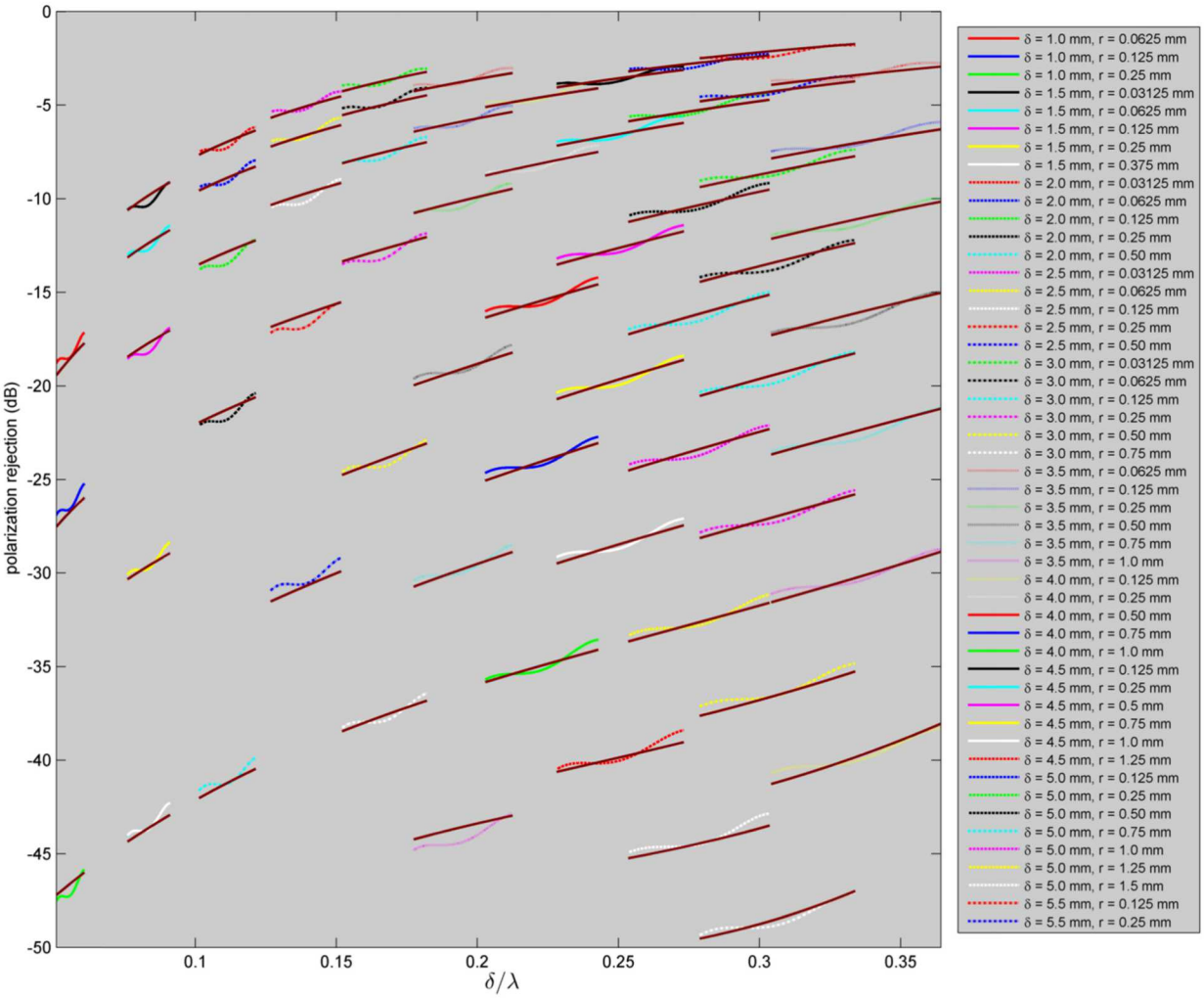

Figure 12 *Cross-polarization transmission data from CST simulations, with smooth curves from the rational fit,* (3)*, over the frequencies* $15.2\ \text{GHz} \le f \le 18.2\ \text{GHz}$. *The legend indicates the parameters of the first 50 simulation data sets in order from left to right and top to bottom.*

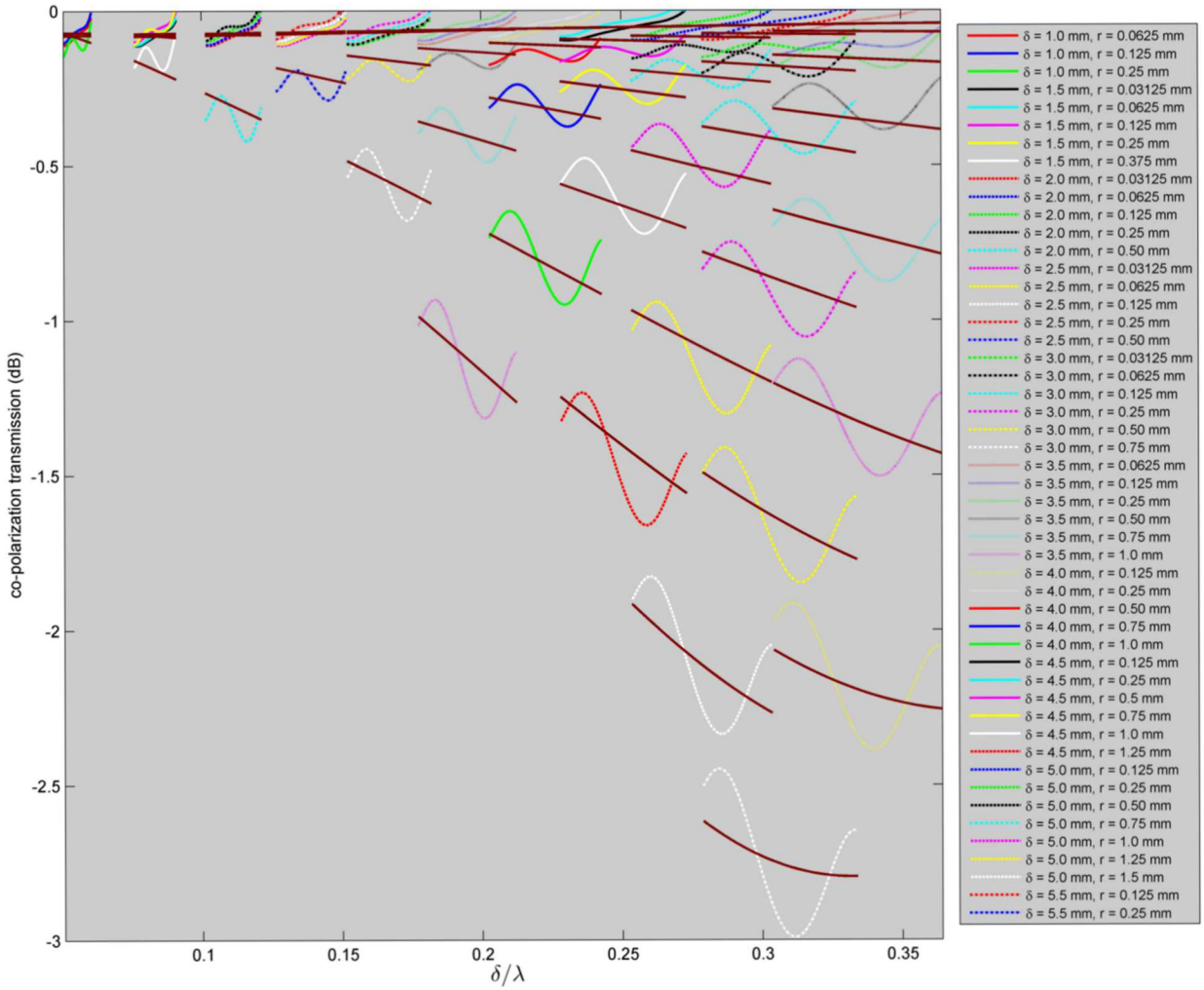

Figure 13 *Co-polarization transmission data from CST simulations, with smooth curves from the rational fit,*(4), *over the frequencies* $15.2\ \text{GHz} \le f \le 18.2\ \text{GHz}$. *The legend indicates the parameters of the first 50 simulation data sets in order from left to right and top to bottom.*

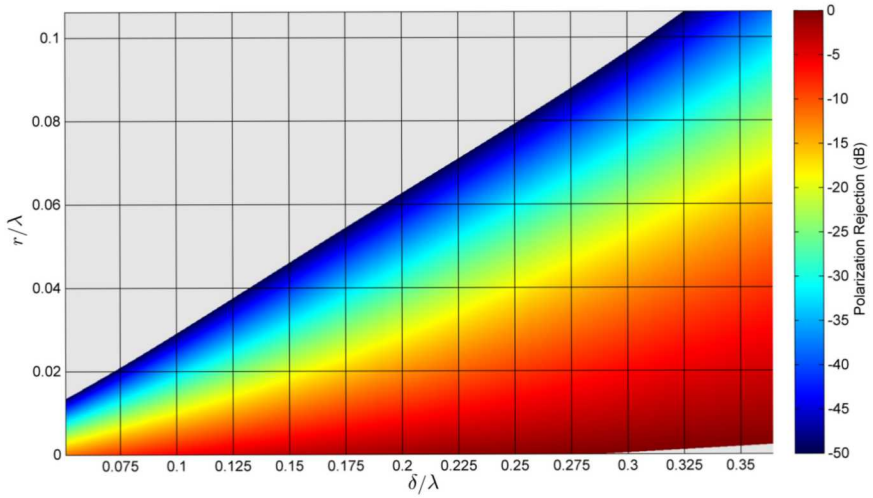

Figure 14 *The region of validity for the rational approximation* (3) *and its estimate of the polarization rejection as a function of normalized wire radius width,* r/λ, *and trace spacing,* δ/λ.

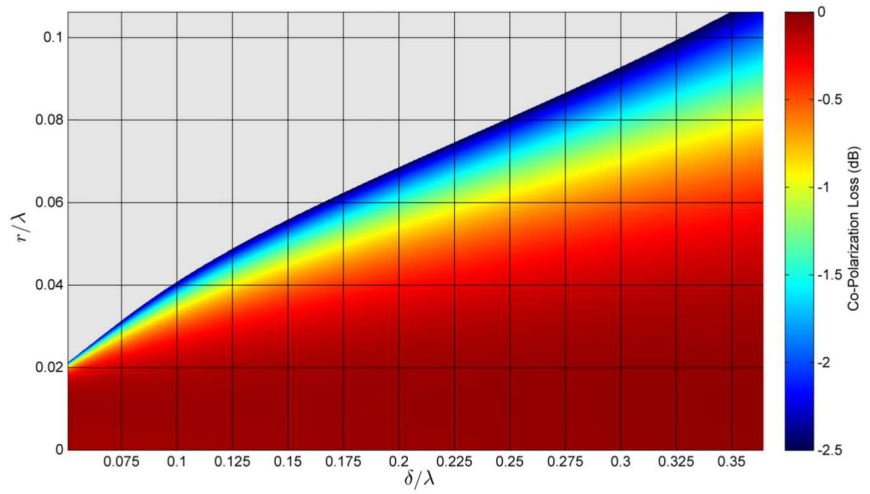

Figure 15 *The region of validity for the rational approximation* (4) *and its estimate of the co-polarization transmission as a function of normalized wire radius width,* r/λ, *and trace spacing,* δ/λ.

For the circuit-trace polarization filter, as with the wire-grid filter, the scale-invariance of Maxwell's equations is invoked to allow a limited set of simulations to be applied over a larger range of dimensions. However, since the circuit-trace filter is built on a thin dielectric sheet, the scaled results from that simulation are only valid when the dielectric properties of the sheet remain the same at the scaled frequency. The two parameters involved in the rational approximation are the width of the trace, w, and the spacing between the trace centers, δ. The thickness of the metal traces is assumed small, as is the thickness of the dielectric, and both are neglected in the parameterized rational approximation of the simulated data. In a strict sense, not scaling these two additional thicknesses violates the scale-invariance of Maxwell's equations, but since both values are intended to remain very small, the usefulness of the approach is not compromised.

For 1/2 oz copper traces (thickness 17 μm) on Rogers RT/duroid® 5880 (thickness 0.254 mm), the following rational approximation to 49 sets of computed polarization-rejection data was obtained,

$$T_{\text{cross-pol}} = \frac{-\frac{505}{6}\left(1+\frac{711}{11}\left(1-\frac{53}{15}\left(1-\frac{31}{37}\frac{w}{\lambda}\right)\frac{w}{\lambda}\right)\frac{w}{\lambda}+\frac{142}{19}\left(1-\frac{85}{13}\frac{\delta}{\lambda}\right)\frac{\delta}{\lambda}\right)}{1-\frac{58}{11}\left(1+\frac{1{,}343}{7}\left(1-\frac{40}{19}\frac{w}{\lambda}\right)\frac{w}{\lambda}\right)\frac{w}{\lambda}+\frac{2{,}151}{17}\left(1+\frac{149}{50}\left(1-\frac{60}{19}\frac{\delta}{\lambda}\right)\frac{\delta}{\lambda}\right)\frac{\delta}{\lambda}} \tag{5}$$

The computed data and the fit from (5) are plotted in Figure 16. As already noted, for this parametric rational approximation, both the thickness of the copper traces and the thickness of the dielectric material are ignored since they are small. The recommended space of r/λ and δ/λ for which (5) gives valid and useful results is shown in Figure 17.

The co-polarization transmission coefficient for the copper-trace polarization filter is estimated by

$$T_{\text{co-pol}} = \frac{-\frac{6}{67}\left(1-\frac{317}{6}\left(1-\frac{966}{47}\left(1+\frac{71}{14}\frac{w}{\lambda}\right)\frac{w}{\lambda}\right)\frac{w}{\lambda}+\frac{947}{22}\frac{\delta}{\lambda}\right)}{1-\frac{83}{2}\left(1+\frac{19}{30}\left(1-\frac{139}{45}\frac{w}{\lambda}\right)\frac{w}{\lambda}\right)\frac{w}{\lambda}+\frac{147}{5}\left(1+\frac{39}{14}\left(1-\frac{50}{33}\frac{\delta}{\lambda}\right)\frac{\delta}{\lambda}\right)\frac{\delta}{\lambda}} \tag{6}$$

The computed data and fit are shown in Figure 18. The recommended space of r/λ and δ/λ where (6) gives valid and useful results is shown in Figure 19. As before, the transmission coefficients are given in decibels by (5) and (6).

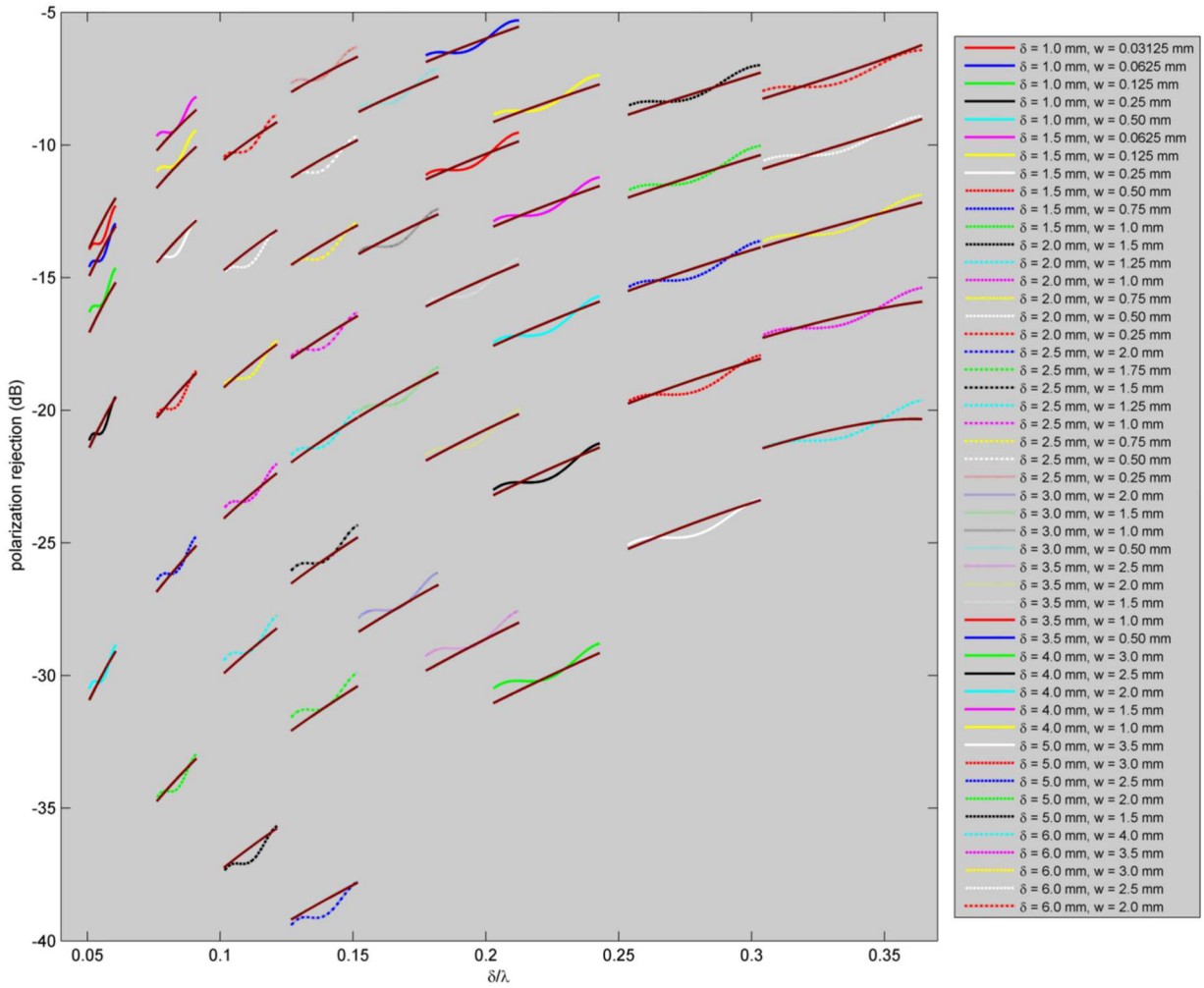

Figure 16 *Cross-polarization rejection data from CST simulations over the frequency range* 15.2 GHz $\leq f \leq$ 18.2 GHz *for various values of trace width and spacing, as indicated in the legend, with approximations from* (5) plotted as dark red smooth lines.

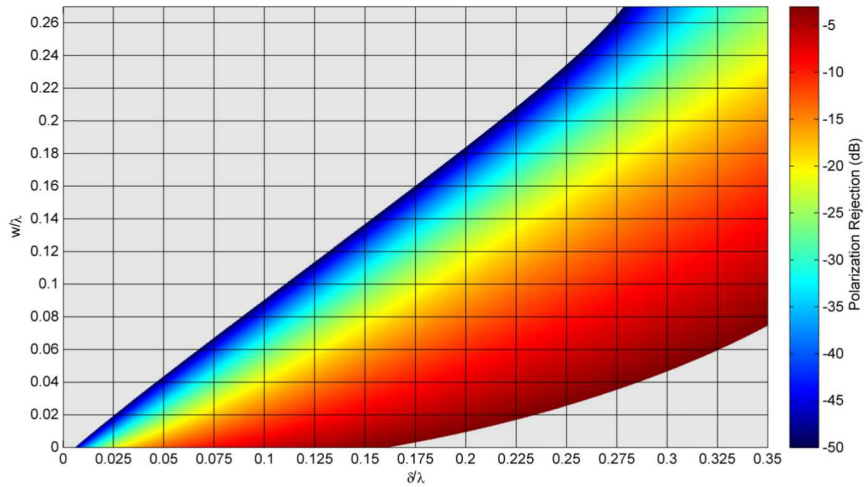

Figure 17 *The region of validity for the rational approximation* (5) *and its estimate of the polarization rejection as a function of normalized trace width,* w/λ *, and trace spacing,* δ/λ *.*

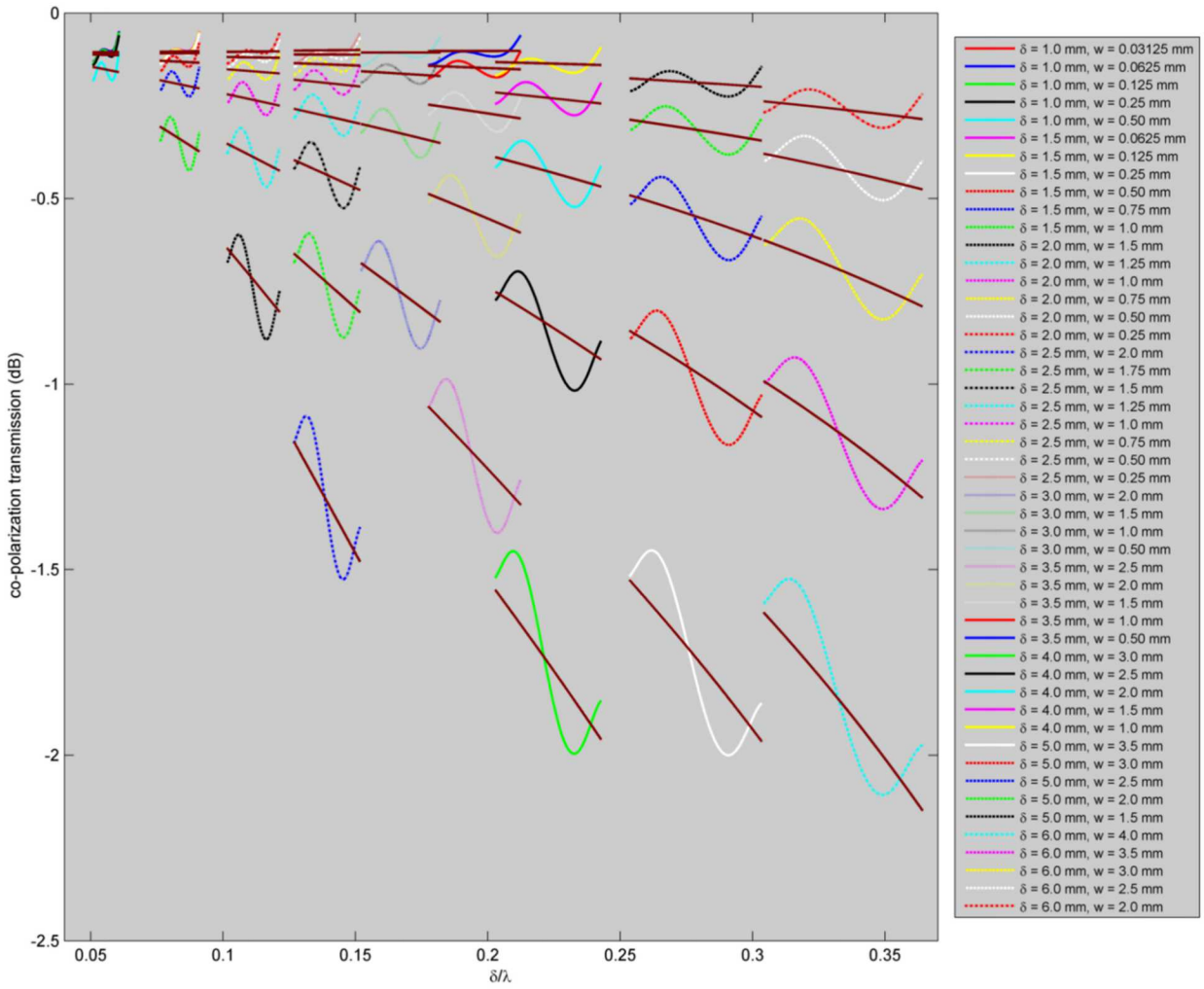

Figure 18 *Co-polarization transmission data from CST simulations over the frequency range* 15.2 GHz $\leq f \leq$ 18.2 GHz *for various values of trace width and spacing, as indicated in the legend, with associated approximations from* (6) plotted as dark red smooth lines.

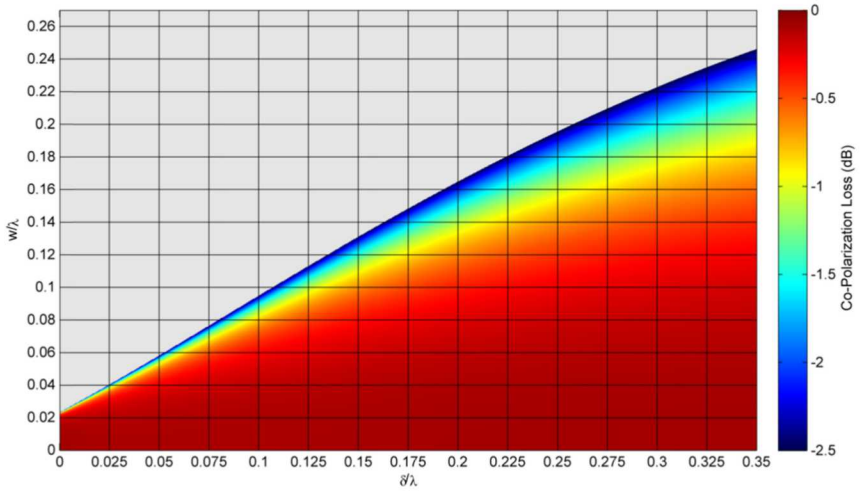

Figure 19 *The region of validity for the rational approximation* (6) *and its estimate of the insertion loss for the desired polarization as a function of normalized trace width,* w/λ *, and trace spacing,* δ/λ *.*

Monopulse response of a dihedral

The monopulse response will be characterized by illuminating a target dihedral with the sum pattern and examining the ratio of the received difference-channel signal to the received sum-channel signal. To allow the examination of the monopulse response over the entire main-lobe region, the dihedral will be placed at each angular position, and the response will be computed as a function of the spherical angles θ, ϕ shown in Figure 2. The corner seam where the dihedral plates join will be rotated by an angle α from the vertical-polarization direction, as illustrated in Figure 6, to achieve different levels of cross-polarization from the target. As described previously, the amount of rotation of the dihedral will control the amount of cross-polarized signal that is received, with $\alpha = 0°$ producing no polarization rotation, and $\alpha = 22.5°$ providing equal amounts of co- and cross-polarized scattering.

The complex scattering matrix (1) is used to compute the received signal. The radiation patterns will be represented by complex partial-gain functions, $h(\theta,\phi)$ and $v(\theta,\phi)$. These complex partial-gain functions carry phase as well as amplitude information, and are related to the partial gains and total gain by

$$\begin{aligned} G_H(\theta,\phi) &= \left|h(\theta,\phi)\right|^2 \\ G_V(\theta,\phi) &= \left|v(\theta,\phi)\right|^2 \\ G(\theta,\phi) &= G_H(\theta,\phi) + G_V(\theta,\phi) \end{aligned} \tag{7}$$

The voltage response at the receive antenna port from the dihedral is

$$\begin{aligned} V_{rx} &= \overbrace{\sqrt{\left(1-\left|\Gamma_{rx}\right|^2\right)\frac{Z_c}{\eta_0}}\frac{\lambda}{2\sqrt{\pi}}\begin{bmatrix} h_{rx}^* & v_{rx}^* \end{bmatrix}}^{\text{vector effective antenna length}} \underbrace{\frac{e^{-jkR}}{2\sqrt{\pi}R}\begin{bmatrix} \gamma_{h,h} & \gamma_{h,v} \\ \gamma_{v,h} & \gamma_{v,v} \end{bmatrix}\overbrace{\begin{bmatrix} h_{tx} \\ v_{tx} \end{bmatrix}\frac{e^{-jkR}}{2\sqrt{\pi}R}\sqrt{\left(1-\left|\Gamma_{tx}\right|^2\right)\frac{\eta_0}{Z_c}}\,V_{tx}}^{\text{electric-field vector at target}}}_{\text{electric-field vector at receiver antenna}}, \\ &= \left[\left(v_{rx}^* v_{tx} - h_{rx}^* h_{tx}\right)\cos 2\alpha + \left(h_{rx}^* v_{tx} + v_{rx}^* h_{tx}\right)\sin 2\alpha\right]\gamma_{dihedral}\frac{e^{-j2kR}}{4\pi R^2}\frac{\lambda}{2\sqrt{\pi}}\sqrt{\left(1-\left|\Gamma_{tx}\right|^2\right)}\,V_{tx} \end{aligned} \tag{8}$$

where R is the range from the radar to the target, Z_c is the characteristic impedance of the transmission line feeding the antenna, η_0 is the impedance of free space, λ is the signal wavelength, $k = 2\pi/\lambda$, $\Gamma_{tx,\,rx}$ are the reflection coefficients at the antenna ports, V_{tx} is the voltage at the transmit antenna port, and $\gamma_{dihedral}$ is the total scattering length of the dihedral, defined so that the radar cross section of the dihedral (area) is $\sigma_{dihedral} = \left|\gamma_{dihedral}\right|^2$.

The unfiltered monopole response is the ratio

$$s(\theta,\phi) = \frac{V_{rx,\,diff}}{V_{rx,\,sum}} = \frac{\left[\left(v_{diff}^* v_{sum} - h_{diff}^* h_{sum}\right)\cos 2\alpha + \left(h_{diff}^* v_{sum} + v_{diff}^* h_{sum}\right)\sin 2\alpha\right]}{\left[\left(v_{sum}^* v_{sum} - h_{sum}^* h_{sum}\right)\cos 2\alpha + \left(h_{sum}^* v_{sum} + v_{sum}^* h_{sum}\right)\sin 2\alpha\right]}, \tag{9}$$

which is complex-valued. Its magnitude gives information about how far the target is from the $\hat{\mathbf{x}}, \hat{\mathbf{z}}$ plane, which contains the boresight direction, and the sign of the argument of the complex value determines in which direction the target is offset. Of course, since this is a single-channel monopulse model, it only provides an angular offset from one plane. When the polarization filter is applied, the ratio becomes

$$s_{filtered}(\theta,\phi) = \frac{V_{rx,\,diff}}{V_{rx,\,sum}} = \frac{\left[\left(T_V v_{diff}^* v_{sum} T_V - T_H h_{diff}^* h_{sum} T_H\right)\cos 2\alpha + \left(T_H h_{diff}^* v_{sum} T_V + T_V v_{diff}^* h_{sum} T_H\right)\sin 2\alpha\right]}{\left[\left(T_V v_{sum}^* v_{sum} T_V - T_H h_{sum}^* h_{sum} T_H\right)\cos 2\alpha + \left(T_H h_{sum}^* v_{sum} T_V + T_V v_{sum}^* h_{sum} T_H\right)\sin 2\alpha\right]}, \tag{10}$$

where the transmission coefficients for the two polarizations are T_V and T_H, and the subscripts V and H refer to the polarization directions corresponding to the complex partial-gain functions, $v(\theta,\phi)$ and $h(\theta,\phi)$, respectively. In the derivation of (10), the assumption is made that the same antenna is used for transmitting and receiving, so that the filter improves the polarization purity of the transmitted signal as well as rejects the cross-polarization component introduced upon scattering from the target.

The magnitude $|s(\theta,\phi)|$ will be plotted with and without the polarization filter for various values of the dihedral rotation angle, α, corresponding to various levels of cross-polarization scattering as shown in Figure 7. Two polarization filters are applied:

1) $T_H = T_{cross-pol.} = -20$ dB and $T_V = T_{co-pol.} = -0.15$ dB, and
2) $T_H = T_{cross-pol.} = -30$ dB and $T_V = T_{co-pol.} = -0.23$ dB.

Figure 20 shows the magnitude of the monopulse response for the first filter, with $\alpha = 0°, 5°, 22.5°,$ and $35°$ from top to bottom. As the amount of cross-polarization in the received signal increases, the unfiltered monopulse response deteriorates. However, the filtered response shows very little deterioration as the cross-polarization increases, even to the point when the co-polarized and cross-polarized signals are equal ($\alpha = 22.5°$). Deterioration is beginning to be noticeable, though, when $\alpha = 35°$, which puts the co-polarized signal nearly 9 dB below the cross-polarized signal, while the unfiltered response shows no indication of the monopulse behavior at all.

If the second filter, with 10 dB better cross-polarization rejection, is applied instead, the monopulse response with $\alpha = 35°$ is almost indistinguishable from the unfiltered response when $\alpha = 0°$. The response with the second filter is plotted in Figure 21 for $\alpha = 35°, 40°, 43°,$ and $44°$ from top to bottom. This filter gives good performance to about $\alpha = 40°$, at which point the cross-polarized response of the dihedral is 15 dB greater than the co-polarized response. Performance deteriorates rapidly for $40° < \alpha \le 45°$, though. With no co-polarized response at $\alpha = 45°$, the monopulse response is completely gone, even with the filter. For these angles and this example, there is no indication of monopulse behavior in the unfiltered response.

As demonstrated by the computed monopulse responses in Figure 20 and Figure 21, the use of a polarization filter dramatically improves the monopulse performance of a short-focal-length offset-fed parabolic reflector.

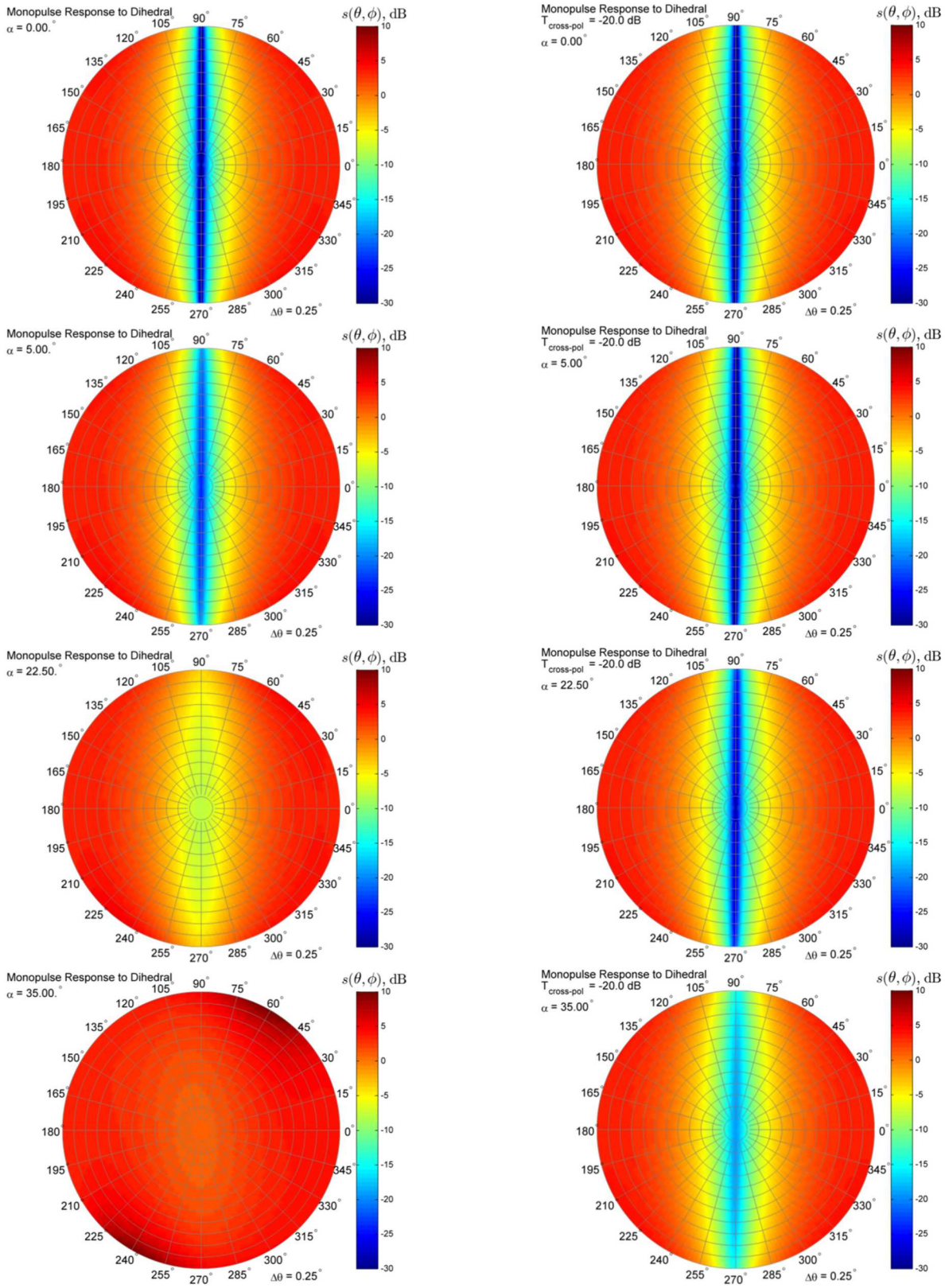

Figure 20 *Monopulse response without polarization filter (left) and with 20 dB cross-polarization rejection filter (right) for several values of the dihedral rotation angle, α. Note that $\alpha > 22.5°$ means that the cross-polarization scattering from the dihedral is stronger than the co-polarization scattering.*

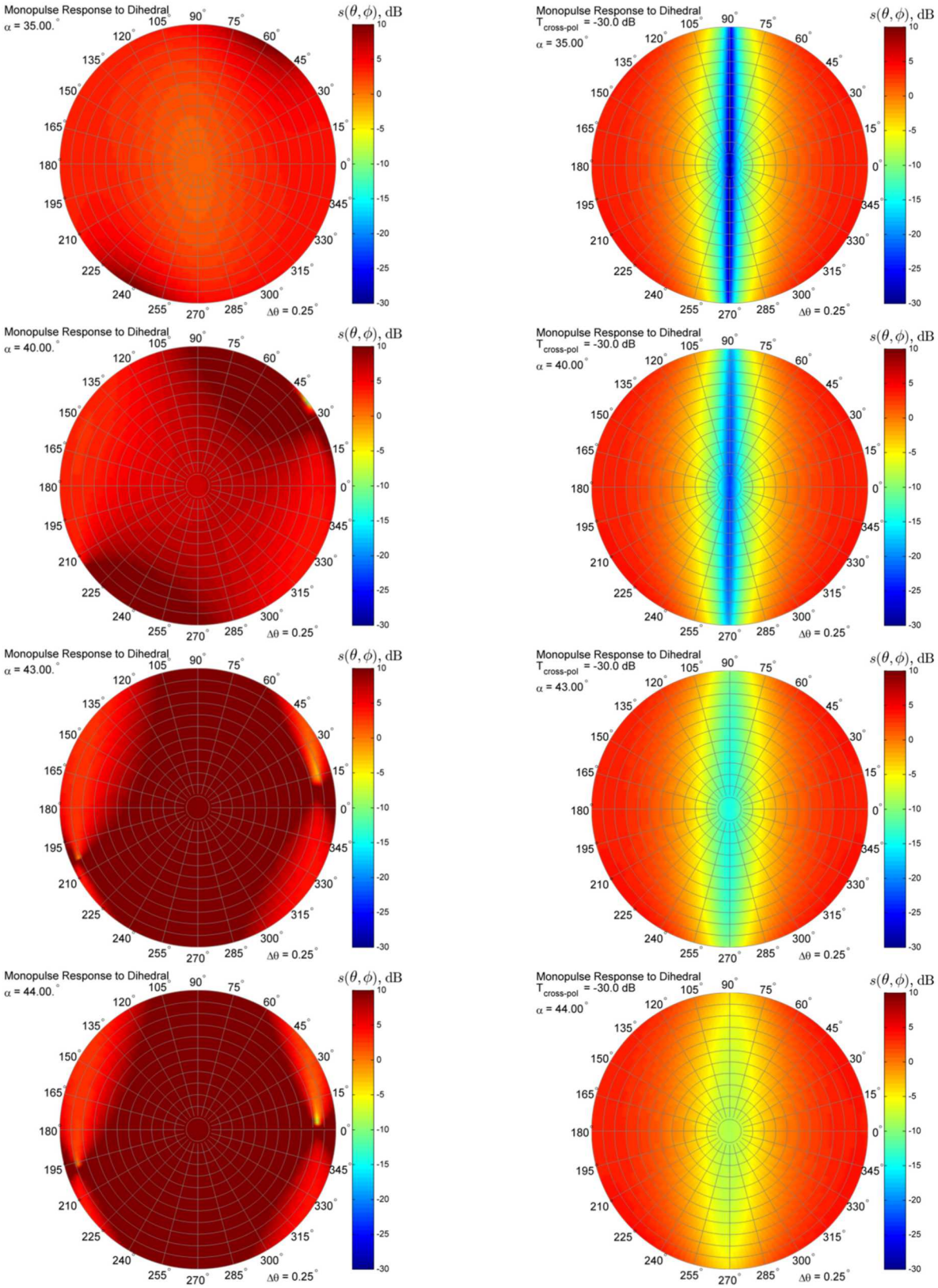

Figure 21 *Monopulse response without polarization filter (left) and with 30 dB cross-polarization rejection filter (right) for* $\alpha = 35°, 40°, 43°, 44°$ *, with significantly stronger cross-polarization scattering compared to the co-polarization scattering.*

Conclusion

We have shown, through the use of computed antenna radiation patterns, that the difference pattern obtained by using a short-focal-length offset-fed parabolic reflector contains significant cross-polarized response in the region of the monopulse null, even producing a local peak where the co-polarized response has a deep null. Using a physical-optics model for the dihedral corner reflector, we also demonstrated that man-made objects containing flat surfaces (or large-radius-of-curvature surfaces) joined along a seam can introduce significant amounts of cross-polarization into the scattered signal. Thus, targets of interest can introduce cross-polarized signals that compete with the expected co-polarized signal in a monopulse system. In addition, multipath scattering from nearby objects, such as surfaces on the aircraft carrying the radar, can enter the system through antenna side lobes, as well as introduce cross-polarized components, and therefor produce unwanted competing signals. Using geometric optics, we illustrated how placing a shroud around the reflector antenna can significantly reduce the multipath interaction with nearby surfaces.

With the dominant contribution to poor monopulse response being the relatively poor cross-polarization response of the difference pattern of the antenna coupled with depolarization by the target, we suggest the use of a polarization filter in front of the antenna. Two kinds of filters are suggested: a wire-grid filter and a filter using circuit traces on a thin dielectric substrate. Using data from a full-wave electromagnetic solver, rational approximations are obtained to allow the easy design of each of these kinds of filters. Generalized formulas, parameterized in normalized filter dimensions, are given for the filter transmission coefficients for both the rejected polarization and the desired polarization directions.

Finally, the fully-polarimetric monopulse response is computed for the example antenna with various amounts of cross-polarization content from the target signal. As the cross-polarization content of the signal scattered from the target increases, the monopulse response of the antenna without the polarization filter deteriorates significantly, quickly becoming unusable. We show that application of the polarization filter dramatically restores the monopulse response, even in conditions where there is no evidence of a monopulse null in the unfiltered response.

Application of the ideas presented here will significantly improve the response of a monopulse system that relies on a short-focal-length offset-fed parabolic reflector.

References

[1] Merrill I. Skolnik, ed., *Introduction to Radar Systems, 2nd edition*, McGraw-Hill Book Co., New York, 1980.

[2] Max Born and Emil Wolf, *Principles of Optics, 7th edition,* Cambridge University Press, Cambridge, 1999.

[3] Merrill I. Skolnik, ed., *Radar Handbook*, McGraw-Hill Book Co., New York, 1970.

[4] Jerry L. Eaves and Edward K. Reedy, *Principles of Modern Radar*, Van Nostrand Reinhold Company, New York, 1987.

[5] Richard C. Johnson and Henry Jasik, ed., *Antenna Engineering Handbook (second edition)*, McGraw-Hill, Inc., New York, 1984.

[6] Y. T. Lo and S. W. Lee ed., *Antenna Handbook, Theory, Applications, and Design*, (Chapter 15, "Reflector Antenna" by Y. Rahmat-Samii), Van Nostrand Reinhold Company, New York, 1988.

[7] CST Studio Suite®, CST Microwave Studio®, CST Computer Simulation Technology AG. Bad Nauheimer Str. 19, 64289 Darmstadt, Germany. (available: http://www.cst.com/)

[8] *AntFarm*™ Antenna Simulation Toolkit, ver. 1.3.3a, Leidos, Inc. (http://www.leidos.com/products/software/antfarm/)

[9] G. T. Ruck, D. E. Barrick, W. D. Stuart, C. K. Krichbaum, *Radar Cross Section Handbook, Volume 2*, Plenum Press, New York, 1970.

[10] Shuen-Yih Wang, Shyh-Kang Jeng, , "A compact RCS formula for a dihedral corner reflector at arbitrary aspect angles," *IEEE Transactions on Antennas and Propagation,* vol.46, no.7, pp.1112-1113, Jul 1998.

[11] T. Griesser, C. Balanis, "Backscatter analysis of dihedral corner reflectors using physical optics and the physical theory of diffraction," *IEEE Transactions on Antennas and Propagation*, vol.35, no.10, pp. 1137- 1147, Oct 1987.

[12] T. Griesser, C. Balanis, "Dihedral corner reflector backscatter using higher order reflections and diffractions," *IEEE Transactions on Antennas and Propagation*, vol.35, no.11, pp. 1235- 1247, Nov 1987

[13] K. W. Sorensen, "A dihedral corner reflector model for full polarization calibration of RCS measurements," *Antennas and Propagation Society International Symposium, 1991. AP-S. Digest*, pp.748-751 vol.2, 24-28 Jun 1991.

[14] Steven E. Allen and Billy C. Brock, "Control of reflected electromagnetic fields at an IFSAR antenna," U. S. Patent 6661368, issued December 9, 2003.

[15] Joseph B. Keller, "Geometrical Diffraction Theory", *Journal of the Optical Society of America*, Vol.52, No. 2, pp.116, Feb 1962.

[16] R.G. Kouyoumjian, P.H. Pathak, "A Uniform Geometrical Theory of Diffraction for an Edge in a Perfectly Conducting Surface", *Proc. IEEE. Vol. 62, pp 1448 -1461, Nov 1974*.

[17] D.A. McNamara, C.W.I Pistorius, J.A.G. Malherbe, *Introduction to the Uniform Geometrical Theory of Diffraction*, Artech House, Boston, 1990.

[18] Constantine A. Balanis, *Advanced Engineering Electromagnetics*, John Wiley & Sons, New York, 1989.

Appendix I – Relationship between polarization vectors

The polarization of an electromagnetic field will refer to the direction of the propagating electric-field vector. Solutions to Maxwell's equations for the propagating electromagnetic field do not allow field components along the direction of propagation, so the propagating field can be described with just two orthogonal vectors, whicht are also mutually orthogonal to the direction of propagation. In the following, several sets of two orthogonal vectors suitable for defining the polarization will be described.

The spherical coordinate system, with the standard spherical unit vectors, is illustrated in Figure I-1. When referencing the spherical coordinate system, the angle θ is usually referred to as the *polar angle*, the *zenith angle*, or the *colatitude*. The angle ϕ is usually referred to as the *azimuth* or the *longitude*. In some usage, the meaning of the two symbols is reversed, and ϕ is used to represent the colatitude and θ represents the longitude, introducing some confusion. Additionally, in the context of an antenna-pattern range, θ is often referred to as the *azimuth* angle even though it is the polar angle measured from the $\hat{\mathbf{z}}$ axis in Figure I-1, and ϕ is referred to as the *roll* angle. In what follows, θ is used for the polar angle, measured from $\hat{\mathbf{z}}$ axis, and ϕ is used for the roll angle, measured in the $\hat{\mathbf{x}},\hat{\mathbf{y}}$ plane, as illustrated in Figure I-1.

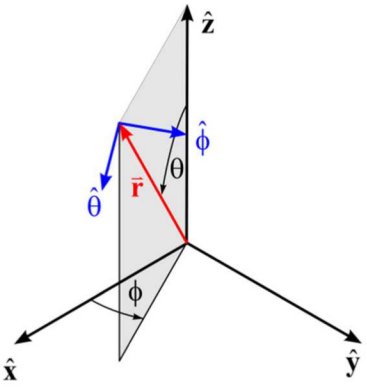

Figure I-1 Spherical coordinate system and the unit vectors.

The field point is located at $\vec{\mathbf{r}} = r\hat{\mathbf{r}}$. The unit vectors $\hat{\mathbf{r}}, \hat{\theta}, \hat{\phi}$ are mutually orthogonal. In the source-free far-field region, the electric field is transverse to the propagation direction (because it has no divergence). If the source is located at the origin, then at position $\vec{\mathbf{r}}$ the field's propagation direction is $\hat{\mathbf{r}}$, so the electric field vector can be described with linear (non-rotating) components along $\hat{\theta}$ and $\hat{\phi}$

$$\vec{\mathbf{E}} = E_\theta \hat{\theta} + E_\phi \hat{\phi} .$$

The polarization of the electromagnetic field, at least within the disciplines of engineering electromagnetics, radar, and antennas, is determined by the direction of the electric-field vector. However, in the discipline of optics, polarization usually refers to the direction of the magnetic-field intensity vector [1, 2]. (One is tempted to say that the subjects of optical and radio-wave propagation differ by 90°.) Here, polarization will always refer to the direction of the electric-field vector.

It will prove convenient to describe the polarization characteristics with the antenna oriented so its bore-sight direction is aligned with the zenith axis, $\hat{\mathbf{z}}$. On occasion, however, the antenna is measured or described in a coordinate system where the bore-sight direction is not so aligned, as illustrated, for example, in Figure I-2. Here the antenna's radiation pattern and polarization vectors are measured in the primed (red) coordinate system. The primed coordinate system can be rotated to become the unprimed coordinate system through the application of a dyadic coordinate-rotation operator to all vectors. Since

more than one rotation is involved, the path from the primed coordinate system to the unprimed system is not unique. However, it will be desirable to make it so.

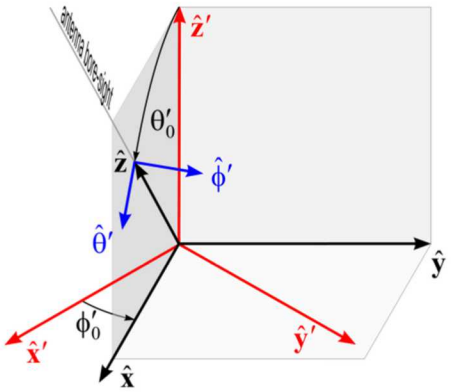

Figure I-2 Two coordinate systems, one aligned with the antenna bore-sight direction, the other not.

Given the right-handed Cartesian coordinate system defined by unit vectors $\hat{\mathbf{x}}', \hat{\mathbf{y}}', \hat{\mathbf{z}}'$ depicted in Figure I-2, the spherical unit vectors are:

$$\hat{\mathbf{r}}' = \hat{\mathbf{x}}'\sin\theta'\cos\phi' + \hat{\mathbf{y}}'\sin\theta'\sin\phi' + \hat{\mathbf{z}}'\cos\theta',$$

$$\hat{\boldsymbol{\theta}}' = \hat{\mathbf{x}}'\cos\theta'\cos\phi' + \hat{\mathbf{y}}'\cos\theta'\sin\phi' - \hat{\mathbf{z}}'\sin\theta', \text{ and} \tag{I-1.1}$$

$$\hat{\boldsymbol{\phi}}' = -\hat{\mathbf{x}}'\sin\phi' + \hat{\mathbf{y}}'\cos\phi'.$$

Suppose a new right-handed Cartesian coordinate system is defined by unit vectors $\hat{\mathbf{x}}, \hat{\mathbf{y}}, \hat{\mathbf{z}}$ with $\hat{\mathbf{z}}$ aligned with the bore-sight direction of the antenna, so that

$$\hat{\mathbf{z}} = \hat{\mathbf{r}}'\left(\theta_0', \phi_0'\right) = \hat{\mathbf{x}}'\sin\theta_0'\cos\phi_0' + \hat{\mathbf{y}}'\sin\theta_0'\sin\phi_0' + \hat{\mathbf{z}}'\cos\theta_0'. \tag{I-1.2}$$

The usual spherical angles will be defined in the unprimed coordinate system, so these new spherical unit vectors are

$$\hat{\mathbf{r}} = \hat{\mathbf{x}}\sin\theta\cos\phi + \hat{\mathbf{y}}\sin\theta\sin\phi + \hat{\mathbf{z}}\cos\theta,$$

$$\hat{\boldsymbol{\theta}} = \hat{\mathbf{x}}\cos\theta\cos\phi + \hat{\mathbf{y}}\cos\theta\sin\phi - \hat{\mathbf{z}}\sin\theta, \text{ and} \tag{I-1.3}$$

$$\hat{\boldsymbol{\phi}} = -\hat{\mathbf{x}}\sin\phi + \hat{\mathbf{y}}\cos\phi.$$

The unit vectors $\hat{\mathbf{x}}$ and $\hat{\mathbf{y}}$ have yet to be defined, and many choices are possible. However, uniqueness is achieved by aligning the spherical unit vectors of the two coordinate systems in the bore-sight direction,

$$\hat{\boldsymbol{\theta}} = \hat{\boldsymbol{\theta}}', \text{ and} \tag{I-1.4}$$

$$\hat{\boldsymbol{\phi}} = \hat{\boldsymbol{\phi}}' \text{ when } \theta = 0, \phi = 0 \text{ and } \theta' = \theta_0', \phi' = \phi_0'. \tag{I-1.5}$$

Thus,

$$\hat{\boldsymbol{\theta}}\Big|_{\substack{\theta=0\\\phi=0}} = \hat{\boldsymbol{\theta}}'\Big|_{\substack{\theta'=\theta_0'\\\phi'=\phi_0'}} = \hat{\mathbf{x}} = \hat{\mathbf{x}}'\cos\theta_0'\cos\phi_0' + \hat{\mathbf{y}}'\cos\theta_0'\sin\phi_0' - \hat{\mathbf{z}}'\sin\theta_0', \text{ and}$$

$$\hat{\boldsymbol{\phi}}\Big|_{\substack{\theta=0\\\phi=0}} = \hat{\boldsymbol{\phi}}'\Big|_{\substack{\theta'=\theta_0'\\\phi'=\phi_0'}} = \hat{\mathbf{y}} = -\hat{\mathbf{x}}'\sin\phi_0' + \hat{\mathbf{y}}'\cos\phi_0'. \tag{I-1.6}$$

Any point $\vec{\mathbf{a}}$ is represented with projections along the primed unit vectors,

$$\vec{\mathbf{a}} = \hat{\mathbf{x}}'a_x' + \hat{\mathbf{y}}'a_y' + \hat{\mathbf{z}}'a_z', \tag{I-1.7}$$

and with projections along the unprimed unit vectors,

$$\vec{\mathbf{a}} = \hat{\mathbf{x}}a_x + \hat{\mathbf{y}}a_y + \hat{\mathbf{z}}a_z. \tag{I-1.8}$$

The projections can also be described by the traditional spherical angles in each of the two coordinate systems, so

$$\bar{\mathbf{a}} = a\left(\hat{\mathbf{x}}'\sin\theta'_a\cos\phi'_a + \hat{\mathbf{y}}'\sin\theta'_a\sin\phi'_a + \hat{\mathbf{z}}'\cos\theta'_a\right), \tag{I-1.9}$$

and

$$\bar{\mathbf{a}} = a\left(\hat{\mathbf{x}}\sin\theta_a\cos\phi_a + \hat{\mathbf{y}}\sin\theta_a\sin\phi_a + \hat{\mathbf{z}}\cos\theta_a\right). \tag{I-1.10}$$

Starting with the identity dyadic,

$$\bar{\bar{\mathbf{I}}} = \hat{\mathbf{x}}\hat{\mathbf{x}} + \hat{\mathbf{y}}\hat{\mathbf{y}} + \hat{\mathbf{z}}\hat{\mathbf{z}},$$

a dyadic coordinate-rotation operator is defined by replacing the vectors on the right with the same vectors represented in the primed coordinate system as follows,

$$\bar{\bar{\mathbf{R}}}^{\hat{\mathbf{x}}'\hat{\mathbf{y}}'\hat{\mathbf{z}}'}_{\hat{\mathbf{x}}\hat{\mathbf{y}}\hat{\mathbf{z}}} = \begin{bmatrix} \hat{\mathbf{x}}\left(\hat{\mathbf{x}}'\cos\theta'_0\cos\phi'_0 + \hat{\mathbf{y}}'\cos\theta'_0\sin\phi'_0 - \hat{\mathbf{z}}'\sin\theta'_0\right) + \\ \hat{\mathbf{y}}\left(-\hat{\mathbf{x}}'\sin\phi'_0 + \hat{\mathbf{y}}'\cos\phi'_0\right) + \\ \hat{\mathbf{z}}\left(\hat{\mathbf{x}}'\sin\theta'_0\cos\phi'_0 + \hat{\mathbf{y}}'\sin\theta'_0\sin\phi'_0 + \hat{\mathbf{z}}'\cos\theta'_0\right) \end{bmatrix}. \tag{I-1.11}$$

Since $\bar{\bar{\mathbf{R}}}^{\hat{\mathbf{x}}'\hat{\mathbf{y}}'\hat{\mathbf{z}}'}_{\hat{\mathbf{x}}\hat{\mathbf{y}}\hat{\mathbf{z}}}$ is a unit dyadic, it does not rotate a vector, but merely transforms the representation from projections along unit vectors from one coordinate system to projections in the other. Specifically, forming the dot product with $\bar{\bar{\mathbf{R}}}^{\hat{\mathbf{x}}'\hat{\mathbf{y}}'\hat{\mathbf{z}}'}_{\hat{\mathbf{x}}\hat{\mathbf{y}}\hat{\mathbf{z}}}$ and any vector on the right represented with projections against $\hat{\mathbf{x}}',\hat{\mathbf{y}}',\hat{\mathbf{z}}'$ returns that same vector, but represented by projections against $\hat{\mathbf{x}},\hat{\mathbf{y}},\hat{\mathbf{z}}$. For vectors represented by projections against $\hat{\mathbf{x}},\hat{\mathbf{y}},\hat{\mathbf{z}}$, the dot product with the vector on the left gives the other representation, or the vector could be placed on the right of the transposed dyadic $\bar{\bar{\mathbf{R}}}^{\hat{\mathbf{x}}\hat{\mathbf{y}}\hat{\mathbf{z}}}_{\hat{\mathbf{x}}'\hat{\mathbf{y}}'\hat{\mathbf{z}}'}$,

$$\bar{\bar{\mathbf{R}}}^{\hat{\mathbf{x}}\hat{\mathbf{y}}\hat{\mathbf{z}}}_{\hat{\mathbf{x}}'\hat{\mathbf{y}}'\hat{\mathbf{z}}'} = \begin{bmatrix} \hat{\mathbf{x}}'\left(\hat{\mathbf{x}}\cos\theta'_0\cos\phi'_0 - \hat{\mathbf{y}}\sin\phi'_0 + \hat{\mathbf{z}}\sin\theta'_0\cos\phi'_0\right) + \\ \hat{\mathbf{y}}'\left(\hat{\mathbf{x}}\cos\theta'_0\sin\phi'_0 + \hat{\mathbf{y}}\cos\phi'_0 + \hat{\mathbf{z}}\sin\theta'_0\sin\phi'_0\right) + \\ \hat{\mathbf{z}}'\left(-\hat{\mathbf{x}}\sin\theta'_0 + \hat{\mathbf{z}}\cos\theta'_0\right) \end{bmatrix}. \tag{I-1.12}$$

Using the subscript $\hat{\mathbf{x}}\hat{\mathbf{y}}\hat{\mathbf{z}}$ or $\hat{\mathbf{x}}'\hat{\mathbf{y}}'\hat{\mathbf{z}}'$ to represent the coordinate axes against which the projections are taken, then the subscripted symbol $\bar{\mathbf{a}}$ can be used to indicate a representation of the vector in either coordinate system, and we have

$$\bar{\mathbf{a}}_{\hat{\mathbf{x}}\hat{\mathbf{y}}\hat{\mathbf{z}}} = \bar{\bar{\mathbf{R}}}^{\hat{\mathbf{x}}'\hat{\mathbf{y}}'\hat{\mathbf{z}}'}_{\hat{\mathbf{x}}\hat{\mathbf{y}}\hat{\mathbf{z}}}\cdot\bar{\mathbf{a}}_{\hat{\mathbf{x}}'\hat{\mathbf{y}}'\hat{\mathbf{z}}'} = \bar{\mathbf{a}}_{\hat{\mathbf{x}}'\hat{\mathbf{y}}'\hat{\mathbf{z}}'}\cdot\bar{\bar{\mathbf{R}}}^{\hat{\mathbf{x}}\hat{\mathbf{y}}\hat{\mathbf{z}}}_{\hat{\mathbf{x}}'\hat{\mathbf{y}}'\hat{\mathbf{z}}'} \text{ and } \bar{\mathbf{a}}_{\hat{\mathbf{x}}'\hat{\mathbf{y}}'\hat{\mathbf{z}}'} = \bar{\bar{\mathbf{R}}}^{\hat{\mathbf{x}}\hat{\mathbf{y}}\hat{\mathbf{z}}}_{\hat{\mathbf{x}}'\hat{\mathbf{y}}'\hat{\mathbf{z}}'}\cdot\bar{\mathbf{a}}_{\hat{\mathbf{x}}\hat{\mathbf{y}}\hat{\mathbf{z}}} = \bar{\mathbf{a}}_{\hat{\mathbf{x}}\hat{\mathbf{y}}\hat{\mathbf{z}}}\cdot\bar{\bar{\mathbf{R}}}^{\hat{\mathbf{x}}'\hat{\mathbf{y}}'\hat{\mathbf{z}}'}_{\hat{\mathbf{x}}\hat{\mathbf{y}}\hat{\mathbf{z}}}, \tag{I-1.13}$$

so that

$$\bar{\mathbf{a}}_{\hat{\mathbf{x}}\hat{\mathbf{y}}\hat{\mathbf{z}}} = \bar{\bar{\mathbf{R}}}^{\hat{\mathbf{x}}'\hat{\mathbf{y}}'\hat{\mathbf{z}}'}_{\hat{\mathbf{x}}\hat{\mathbf{y}}\hat{\mathbf{z}}}\cdot\bar{\mathbf{a}}_{\hat{\mathbf{x}}'\hat{\mathbf{y}}'\hat{\mathbf{z}}'} = \bar{\bar{\mathbf{R}}}^{\hat{\mathbf{x}}'\hat{\mathbf{y}}'\hat{\mathbf{z}}'}_{\hat{\mathbf{x}}\hat{\mathbf{y}}\hat{\mathbf{z}}}\cdot\left(\bar{\bar{\mathbf{R}}}^{\hat{\mathbf{x}}\hat{\mathbf{y}}\hat{\mathbf{z}}}_{\hat{\mathbf{x}}'\hat{\mathbf{y}}'\hat{\mathbf{z}}'}\cdot\bar{\mathbf{a}}_{\hat{\mathbf{x}}\hat{\mathbf{y}}\hat{\mathbf{z}}}\right), \tag{I-1.14}$$

implying

$$\bar{\bar{\mathbf{R}}}^{\hat{\mathbf{x}}'\hat{\mathbf{y}}'\hat{\mathbf{z}}'}_{\hat{\mathbf{x}}\hat{\mathbf{y}}\hat{\mathbf{z}}}\cdot\bar{\bar{\mathbf{R}}}^{\hat{\mathbf{x}}\hat{\mathbf{y}}\hat{\mathbf{z}}}_{\hat{\mathbf{x}}'\hat{\mathbf{y}}'\hat{\mathbf{z}}'} = \hat{\mathbf{x}}\hat{\mathbf{x}} + \hat{\mathbf{y}}\hat{\mathbf{y}} + \hat{\mathbf{z}}\hat{\mathbf{z}}, \tag{I-1.15}$$

which is easily verified by direct computation with (I-1.11) and (I-1.12).

Applying the coordinate-rotation operator to the representations of a vector described by the angles θ',ϕ' and θ,ϕ in the two coordinate systems, it can readily be determined that the angles are related by

$$\begin{aligned} \sin\theta\cos\phi &= \sin\theta'\cos\theta'_0\cos\left(\phi'-\phi'_0\right) - \cos\theta'\sin\theta'_0 \\ \sin\theta\sin\phi &= \sin\theta'\sin\left(\phi'-\phi'_0\right) \\ \cos\theta &= \sin\theta'\sin\theta'_0\cos\left(\phi'-\phi'_0\right) + \cos\theta'\cos\theta'_0 \end{aligned} \tag{I-1.16}$$

and

$$\begin{aligned}
\sin\theta'\cos\phi' &= \sin\theta\cos\theta_0'\cos\phi\cos\phi_0' - \sin\theta\sin\phi\sin\phi_0' + \cos\theta\sin\theta_0'\cos\phi_0' \\
\sin\theta'\sin\phi' &= \sin\theta\cos\theta_0'\cos\phi\sin\phi_0' + \sin\theta\sin\phi\cos\phi_0' + \cos\theta\sin\theta_0'\sin\phi_0' \\
\cos\theta' &= \cos\theta\cos\theta_0' - \sin\theta\sin\theta_0'\cos\phi
\end{aligned} \tag{I-1.17}$$

Equations (I-1.16) lead to expressions for the spherical angles in the unprimed coordinate system,

$$\theta = \cos^{-1}\left(\sin\theta'\sin\theta_0'\cos\left(\phi' - \phi_0'\right) + \cos\theta'\cos\theta_0'\right), \tag{I-1.18}$$

and

$$\phi = \tan^{-1}\left(\frac{\sin\theta'\sin\left(\phi' - \phi_0'\right)}{\sin\theta'\cos\theta_0'\cos\left(\phi' - \phi_0'\right) - \cos\theta'\sin\theta_0'}\right), \tag{I-1.19}$$

while equations (I-1.17) provide expressions for the angles in the primed coordinate system,

$$\theta' = \cos^{-1}\left(\cos\theta\cos\theta_0' - \sin\theta\sin\theta_0'\cos\phi\right), \tag{I-1.20}$$

and

$$\phi' = \tan^{-1}\left(\frac{\sin\theta\left(\cos\theta_0'\cos\phi\sin\phi_0' + \sin\phi\cos\phi_0'\right) + \cos\theta\sin\theta_0'\sin\phi_0'}{\sin\theta\left(\cos\theta_0'\cos\phi\cos\phi_0' - \sin\phi\sin\phi_0'\right) + \cos\theta\sin\theta_0'\cos\phi_0'}\right). \tag{I-1.21}$$

The visualization of the various vectors in the two coordinate systems is aided by Figure I-3, where the unprimed coordinate system (black) has been rotated with respect to the primed system (red) according to the description above. In this illustration, $\theta_0' = 30°$, and $\phi_0' = 45°$.

The unit vectors in the radial direction are the same in both coordinate systems, so $\hat{\mathbf{r}} = \hat{\mathbf{r}}'$. Note that the unit vector in the direction of increasing θ, $\hat{\boldsymbol{\theta}}$, lies in the plane defined by $\hat{\mathbf{r}}$ and $\hat{\mathbf{z}}$. However, the corresponding vector in the primed system, $\hat{\boldsymbol{\theta}}'$ lies in the plane defined by $\hat{\mathbf{r}}$ and $\hat{\mathbf{z}}'$. The remaining unit vectors, $\hat{\boldsymbol{\phi}}$ and $\hat{\boldsymbol{\phi}}'$, are normal to these planes, respectively. The important point is that, while $\hat{\boldsymbol{\theta}} = \hat{\boldsymbol{\theta}}'$ and $\hat{\boldsymbol{\phi}} = \hat{\boldsymbol{\phi}}'$ when $\hat{\mathbf{r}} = \hat{\mathbf{r}}' = \hat{\mathbf{z}}$, $\hat{\boldsymbol{\theta}} \neq \hat{\boldsymbol{\theta}}'$ and $\hat{\boldsymbol{\phi}} \neq \hat{\boldsymbol{\phi}}'$ in general. Since these unit vectors correspond to the direction of the electric-field components E_θ and E_ϕ, the polarization components will match in the bore-sight direction, but they will be different in the two representations as the field point moves away from the bore-sight direction. The difference between the two representations increases as the distance from the bore-sight increases.

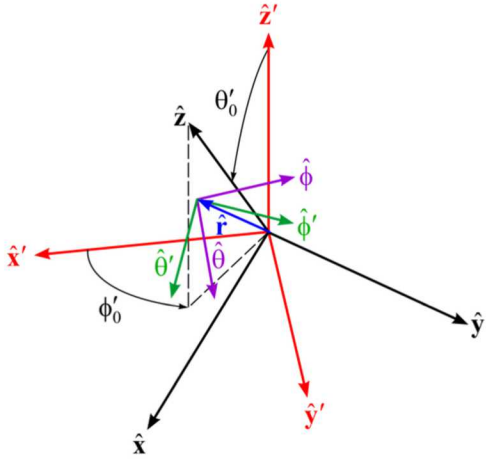

Figure I-3 Illustration of the various vectors in two Cartesian coordinate systems rotated with respect to each other.

The unit vectors ($\hat{\theta}', \hat{\phi}'$ and $\hat{\theta}, \hat{\phi}$) that describe the polarization of the electric field all lie in the same plane, since they are perpendicular to the same radial vector. The relationship between these vectors is best described with a single rotation angle. Let the angle between $\hat{\theta}$ and $\hat{\theta}'$ be α, so that

$$\hat{\theta} = \hat{\theta}'\cos\alpha + \hat{\phi}'\sin\alpha, \text{ and } \hat{\phi} = -\hat{\theta}'\sin\alpha + \hat{\phi}'\cos\alpha . \tag{I-1.22}$$

The angle α is obtained in all quadrants by

$$\alpha = \tan^{-1}\left(\frac{\hat{\theta}\cdot\hat{\phi}'}{\hat{\theta}\cdot\hat{\theta}'}\right), \tag{I-1.23}$$

or

$$\alpha = \tan^{-1}\left(\frac{\sin\theta_0 \sin(\phi' - \phi_0)}{\cos\theta_0 \sin\theta' - \sin\theta_0 \cos\theta' \cos(\phi' - \phi_0)}\right). \tag{I-1.24}$$

The mapping of the spherical angles in the primed coordinate system given by (I-1.18) and (I-1.19) is illustrated in Figure I-4 for $\theta'_0 = 30°$, and $\phi'_0 = 45°$. The contours plotted in Figure I-4 show the entire spherical region and allow values to be read with some ease. These plots clearly illustrate the non-linear nature of the mapping, and with some thought, the location of the poles in the new, unprimed coordinate system can be recognized. However, when the same data are plotted on the surface of a sphere, as in Figure I-5, it becomes clear that this mapping is precisely what intuition expects. In these plots, it is assumed that $0 \le \phi, \phi' \le 360°$

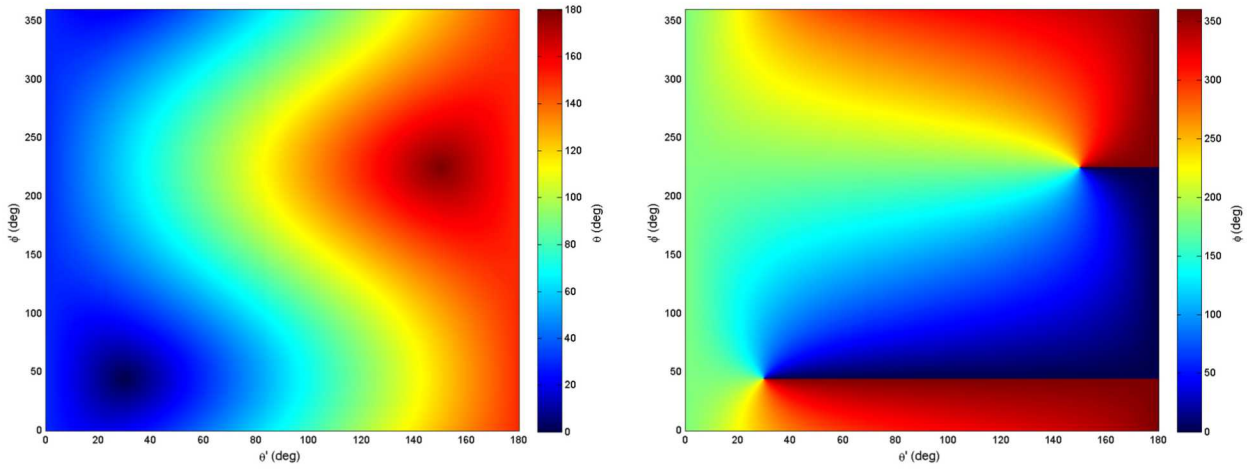

Figure I-4 Mapping of the spherical angles, θ′ and ϕ′, in the primed coordinate system to the corresponding angles in the unprimed coordinate system, with θ on the left, and ϕ on the right.

The rotation angle, α, between the polarization unit vectors, given by (I-1.24), behaves similarly to ϕ, but not identically. Figure I-6 shows α as a function of the position in the primed coordinate system when $\theta'_0 = 30°$, and $\phi'_0 = 45°$. When the coordinate system must be moved to correspond to the bore-sight direction of the antenna, it is important that the polarization basis vectors be rotated as required, according to (I-1.22) and (I-1.24). While the rotation is obviously necessary for the linear basis ($\hat{\theta}, \hat{\phi}$) described here, it is also necessary when the field is represented by circularly polarized unit vectors. However, in this case, rotation affects the phase .

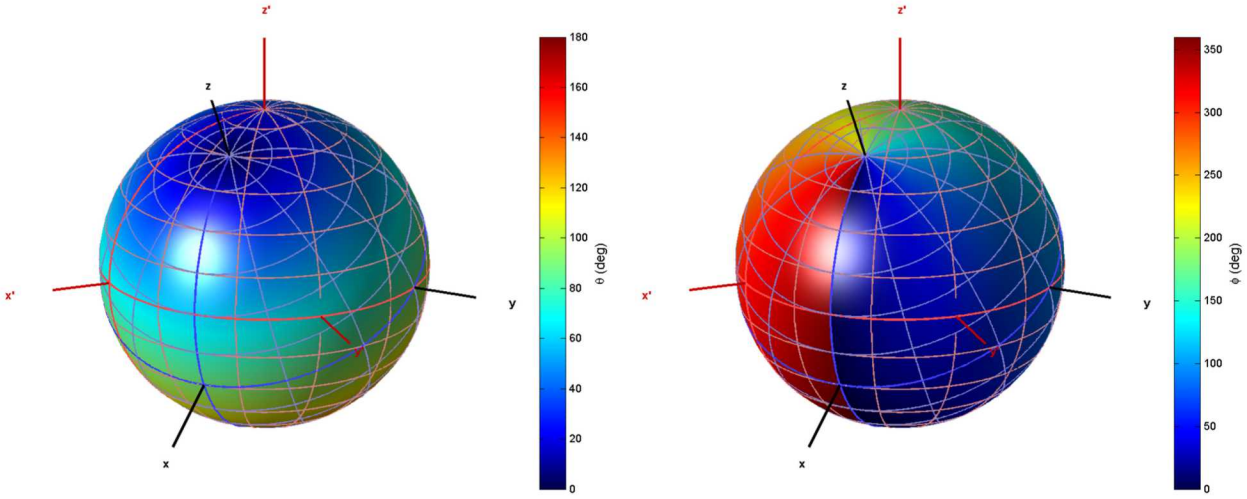

Figure I-5 Illustration of the mapping onto the surface of a sphere of the spherical angles, θ′ and ϕ′, in the primed coordinate system to the corresponding angles in the unprimed coordinate system. The primed coodinate system is designated with the red axes, and the unprimed coordinate system has black axes. θ is mapped on the left sphere, and ϕ is on the right. Lines of constant lattitude and longitude are plotted for both coordinate systems.

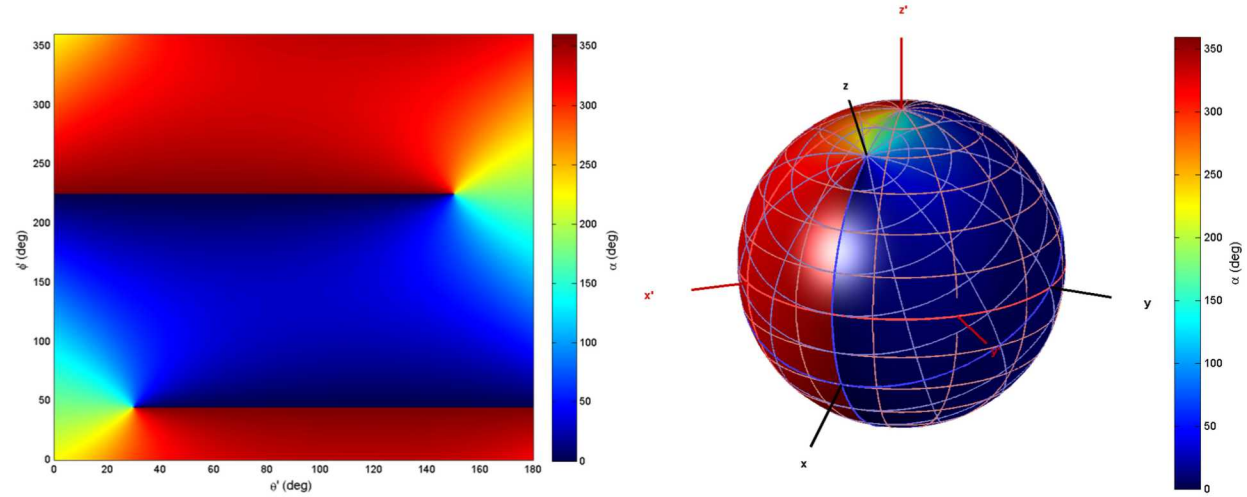

Figure I-6 Illustration of the behavior of the angle between the spherical unit vectors, $\hat{\theta}$ and $\hat{\theta}'$ (or $\hat{\phi}$ and $\hat{\phi}'$) in the two coordinate systems as a function of primed coordinates, θ' and ϕ'.

The components, E_θ and E_ϕ, are often the most convenient linearly polarized components for use in analysis and computation, since they represent electric-field components along the unit vectors in the spherical coordinate system. However, other linear polarizations are also commonly used, as well as rotating components. Particularly useful linear polarization basis sets, defined by A. Ludwig, will be described next.

The linear polarizations defined by A. Ludwig

In an effort to define linear polarization components that could be useful for describing the principal- and cross-polarization radiation patterns of an antenna, Arthur Ludwig proposed three definitions for

orthogonal pairs of linear polarization components [17]. Figure I-1 and Figure I-7 illustrate a standard coordinate system used to describe radiation patterns from an antenna. In Figure I-7, the coordinate system is viewed from the perspective of a planar near-field range, where the $\hat{\mathbf{z}}$ axis points toward, and is normal to, the scan plane, which is parallel to the $\hat{\mathbf{x}},\hat{\mathbf{y}}$ axis and located at $z = z_0$. The antenna is located at the origin, typically, but not necessarily, with its main radiation lobe pointed along the $\hat{\mathbf{z}}$ axis.

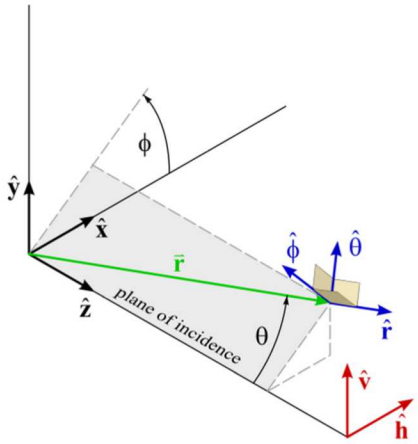

Figure I-7 Illustration of the reference coordinate system, showing the standard spherical angles and unit vectors at position $\vec{\mathbf{r}}$. The vectors $\hat{\mathbf{v}}, \hat{\mathbf{h}}$ are the Ludwig-polarization unit vectors (all definitions) at position $\theta = 0, \phi = 0$.

The electric field vectors at a point $\vec{\mathbf{r}}$ can be described with components along the spherical unit vectors $\hat{\mathbf{r}}, \hat{\boldsymbol{\theta}}$ and $\hat{\boldsymbol{\phi}}$, given in terms of the Cartesian unit vectors as

$$\begin{aligned} \hat{\mathbf{r}} &= \hat{\mathbf{x}}\sin\theta\cos\phi + \hat{\mathbf{y}}\sin\theta\sin\phi + \hat{\mathbf{z}}\cos\theta \\ \hat{\boldsymbol{\theta}} &= \hat{\mathbf{x}}\cos\theta\cos\phi + \hat{\mathbf{y}}\cos\theta\sin\phi - \hat{\mathbf{z}}\sin\theta\,. \\ \hat{\boldsymbol{\phi}} &= -\hat{\mathbf{x}}\sin\phi + \hat{\mathbf{y}}\cos\phi \end{aligned} \tag{I-2.1}$$

In the source-free region, the propagating field will have no divergence and thus no component along $\hat{\mathbf{r}}$. A plane of incidence is defined by $\hat{\mathbf{z}}$ and $\hat{\mathbf{r}}$. Since $\hat{\mathbf{z}} \times \hat{\mathbf{r}} = \hat{\boldsymbol{\phi}}\sin\theta$, it is clear that $\hat{\boldsymbol{\phi}}$ is normal to this plane of incidence. Since $\hat{\boldsymbol{\theta}}$ is normal to both $\hat{\boldsymbol{\phi}}$ and $\hat{\mathbf{r}}$, it must lie in the plane of incidence.

The three definitions proposed by Ludwig define pairs of linear polarizations, which will be designated here as $\hat{\mathbf{v}}, \hat{\mathbf{h}}$. Where appropriate, a subscript will be used to indicate which of Ludwig's definitions is being represented. These polarization unit vectors are illustrated in Figure I-7 at position $\theta = 0, \phi = 0$, where the corresponding components from all three definitions are the same. Below, the definitions will be given in terms of the spherical unit vectors and the Cartesian unit vectors.

Definition 1

Ludwig's first definition is [17]

$$\begin{aligned} \hat{\mathbf{v}}_1 &= \hat{\mathbf{r}}\sin\theta\sin\phi + \hat{\boldsymbol{\theta}}\cos\theta\sin\phi + \hat{\boldsymbol{\phi}}\cos\phi = \hat{\mathbf{y}} \\ \hat{\mathbf{h}}_1 &= \hat{\mathbf{r}}\sin\theta\cos\phi + \hat{\boldsymbol{\theta}}\cos\theta\cos\phi - \hat{\boldsymbol{\phi}}\sin\phi = \hat{\mathbf{x}} \end{aligned} \tag{I-2.2}$$

Note that these unit vectors cannot completely describe the electric-field vector propagating in any direction other than $\theta = 0$, since the propagating electric field must be perpendicular to the direction of propagation. When $\theta \neq 0$, this would require a component along $\hat{\mathbf{z}}$ for at least one of the components. The fact that this polarization basis is incomplete would seem to limit the usefulness of definition 1.

However, given the fact that the electric field has no divergence in the source-free region, the complete polarization can be derived from the Ludwig-1 components. Thus,

$$\begin{aligned}\nabla\cdot\vec{\mathbf{E}} = 0 &= \nabla\cdot\left(\hat{\mathbf{x}}E_x + \hat{\mathbf{y}}E_y + \hat{\mathbf{z}}E_z\right)e^{-j\vec{\mathbf{k}}\cdot\vec{\mathbf{r}}} \\ &= k_xE_x + k_yE_y + k_zE_z\end{aligned} \tag{I-2.3}$$

so

$$E_z = -\frac{k_xE_x + k_yE_y}{\sqrt{k^2 - k_x^2 - k_y^2}}, \tag{I-2.4}$$

where $\vec{\mathbf{k}} = k\hat{\mathbf{r}}$ and $k = 2\pi f/c$ where f is the frequency in Hz and c is the speed of light, 299,792,458 m/s in the vacuum.

Definition 2

Ludwig's second definition is [17]

$$\begin{aligned}\hat{\mathbf{v}}_2 &= \frac{\hat{\boldsymbol{\theta}}\cos\theta\sin\phi + \hat{\boldsymbol{\phi}}\cos\phi}{\sqrt{1-\sin^2\theta\sin^2\phi}} = \frac{-\hat{\mathbf{x}}\sin^2\theta\sin\phi\cos\phi + \hat{\mathbf{y}}\left(1-\sin^2\theta\sin^2\phi\right) - \hat{\mathbf{z}}\sin\theta\cos\theta\sin\phi}{\sqrt{1-\sin^2\theta\sin^2\phi}} \\ \hat{\mathbf{h}}_2 &= \frac{\hat{\boldsymbol{\theta}}\cos\phi - \hat{\boldsymbol{\phi}}\cos\theta\sin\phi}{\sqrt{1-\sin^2\theta\sin^2\phi}} = \frac{\hat{\mathbf{x}}\cos\theta - \hat{\mathbf{z}}\sin\theta\cos\phi}{\sqrt{1-\sin^2\theta\sin^2\phi}}\end{aligned} \tag{I-2.5}$$

and the spherical unit vectors can be obtained as

$$\begin{aligned}\hat{\boldsymbol{\theta}} &= \frac{\hat{\mathbf{v}}_2\cos\theta\sin\phi + \hat{\mathbf{h}}_2\cos\phi}{\sqrt{1-\sin^2\theta\sin^2\phi}} \\ \hat{\boldsymbol{\phi}} &= \frac{\hat{\mathbf{v}}_2\cos\phi - \hat{\mathbf{h}}_2\cos\theta\sin\phi}{\sqrt{1-\sin^2\theta\sin^2\phi}}\end{aligned}. \tag{I-2.6}$$

The Ludwig-2 polarization can also be written

$$\begin{aligned}\hat{\mathbf{v}}_2 &= \hat{\boldsymbol{\theta}}\sin\zeta + \hat{\boldsymbol{\phi}}\cos\zeta \\ \hat{\mathbf{h}}_2 &= \hat{\boldsymbol{\theta}}\cos\zeta - \hat{\boldsymbol{\phi}}\sin\zeta\end{aligned}, \tag{I-2.7}$$

where

$$\zeta = \tan^{-1}\left(\frac{\cos\theta\sin\phi}{\cos\phi}\right). \tag{I-2.8}$$

This polarization definition essentially uses the spherical unit vectors in a new coordinate system defined by $\hat{\mathbf{x}}' = \hat{\mathbf{x}}$, $\hat{\mathbf{y}}' = \hat{\mathbf{z}}$, and $\hat{\mathbf{z}}' = -\hat{\mathbf{y}}$. In the new coordinate system, $\hat{\mathbf{v}}_2 = \hat{\boldsymbol{\theta}}'$ and $\hat{\mathbf{h}}_2 = \hat{\boldsymbol{\phi}}'$. However, as expressed in the coordinate system in Figure I-1, these vectors have problems at the points $\theta = \pi/2$, $\phi = \pi/2, 3\pi/2$, where

$$\begin{aligned}\hat{\mathbf{v}}_2\left(\theta = \frac{\pi}{2}+\gamma, \phi = \frac{\pi}{2}+\delta\right) &= \hat{\mathbf{v}}_2\left(\theta = \frac{\pi}{2}+\gamma, \phi = \frac{3\pi}{2}+\delta\right) \\ &= \hat{\mathbf{x}}\frac{\cos^2\gamma\cos\delta\sin\delta}{\sqrt{1-\cos^2\gamma\cos^2\delta}} + \hat{\mathbf{y}}\frac{\sin^2\gamma\cos^2\delta + \sin^2\delta}{\sqrt{1-\cos^2\gamma\cos^2\delta}} + \hat{\mathbf{z}}\frac{\cos\gamma\sin\gamma\cos\delta}{\sqrt{1-\cos^2\gamma\cos^2\delta}}\end{aligned} \tag{I-2.9}$$

and

$$\hat{\mathbf{h}}_2\left(\theta = \frac{\pi}{2}+\gamma, \phi = \frac{\pi}{2}+\delta\right) = -\hat{\mathbf{x}}\frac{\sin\gamma}{\sqrt{1-\cos^2\gamma\cos^2\delta}} + \hat{\mathbf{z}}\frac{\cos\gamma\sin\delta}{\sqrt{1-\cos^2\gamma\cos^2\delta}} \tag{I-2.10}$$

while

$$\hat{\mathbf{h}}_2\left(\theta=\frac{\pi}{2}+\gamma,\phi=\frac{3\pi}{2}+\delta\right)=-\hat{\mathbf{x}}\frac{\sin\gamma}{\sqrt{1-\cos^2\gamma\cos^2\delta}}-\hat{\mathbf{z}}\frac{\cos\gamma\sin\delta}{\sqrt{1-\cos^2\gamma\cos^2\delta}} \tag{I-2.11}$$

The vectors are different, depending on the path taken to arrive at the point, for example

$$\lim_{\delta\to 0}\left(\hat{\mathbf{v}}_2\left(\theta=\frac{\pi}{2},\phi=\frac{\pi}{2}+\delta\right)\right)=\hat{\mathbf{x}}\,\mathrm{sgn}(\delta), \tag{I-2.12}$$

while

$$\lim_{\gamma\to 0}\hat{\mathbf{v}}_2\left(\theta=\frac{\pi}{2}+\gamma,\phi=\frac{\pi}{2}\right)=\hat{\mathbf{z}}. \tag{I-2.13}$$

Similarly,

$$\lim_{\delta\to 0}\left(\hat{\mathbf{h}}_2\left(\theta=\frac{\pi}{2},\phi=\frac{\pi}{2}+\delta\right)\right)=-\hat{\mathbf{z}}\,\mathrm{sgn}(\delta), \tag{I-2.14}$$

while

$$\lim_{\gamma\to 0}\hat{\mathbf{h}}_2\left(\theta=\frac{\pi}{2}+\gamma,\phi=\frac{\pi}{2}\right)=-\hat{\mathbf{x}}. \tag{I-2.15}$$

Since the limits depend on the direction of approach, the vectors do not exist at $\theta=\pi/2$ and $\phi=\pi/2,3\pi/2$.

Definition 3

Ludwig's third definition is [17]

$$\begin{aligned}\hat{\mathbf{v}}_3&=\hat{\boldsymbol{\theta}}\sin\phi+\hat{\boldsymbol{\phi}}\cos\phi=-\hat{\mathbf{x}}(1-\cos\theta)\sin\phi\cos\phi+\hat{\mathbf{y}}\left(1-\sin^2\phi(1-\cos\theta)\right)-\hat{\mathbf{z}}\sin\theta\sin\phi\\ \hat{\mathbf{h}}_3&=\hat{\boldsymbol{\theta}}\cos\phi-\hat{\boldsymbol{\phi}}\sin\phi=\hat{\mathbf{x}}\left(1-\cos^2\phi(1-\cos\theta)\right)-\hat{\mathbf{y}}(1-\cos\theta)\sin\phi\cos\phi-\hat{\mathbf{z}}\sin\theta\cos\phi\end{aligned}, \tag{I-2.16}$$

and

$$\begin{aligned}\hat{\boldsymbol{\theta}}&=\hat{\mathbf{v}}_3\sin\phi+\hat{\mathbf{h}}_3\cos\phi\\ \hat{\boldsymbol{\phi}}&=\hat{\mathbf{v}}_3\cos\phi-\hat{\mathbf{h}}_3\sin\phi\end{aligned}. \tag{I-2.17}$$

To measure this polarization with a roll-over-azimuth positioner, where the roll angle is equivalent to the spherical coordinate ϕ and the azimuth angle is equivalent to spherical coordinate θ, the dual-linear probe antenna would necessarily rotate in synchrony with the antenna being tested.

Other similar polarization representations

It is interesting to see that the relation between the pair $\hat{\mathbf{v}}_2,\hat{\mathbf{h}}_2$ and the pair $\hat{\boldsymbol{\theta}},\hat{\boldsymbol{\phi}}$ is identical to the inverse relation between the pair $\hat{\boldsymbol{\theta}},\hat{\boldsymbol{\phi}}$ and the pair $\hat{\mathbf{v}}_2,\hat{\mathbf{h}}_2$. Similarly, the transformation from the pair $\hat{\mathbf{v}}_3,\hat{\mathbf{h}}_3$ to the pair $\hat{\boldsymbol{\theta}},\hat{\boldsymbol{\phi}}$ is the same as the inverse transformation. This property, known as involution, is exhibited by some other pairs of unit vectors relative to the pair $\hat{\boldsymbol{\theta}},\hat{\boldsymbol{\phi}}$. These other pairs are described by a single parameter, *a*, as follows

$$\begin{aligned}\hat{\mathbf{v}}_a&=\hat{\boldsymbol{\theta}}a\pm\hat{\boldsymbol{\phi}}\sqrt{1-a^2}\\ \hat{\mathbf{h}}_a&=\pm\hat{\boldsymbol{\theta}}\sqrt{1-a^2}-\hat{\boldsymbol{\phi}}a\end{aligned} \tag{I-2.18}$$

and

$$\begin{aligned}\hat{\boldsymbol{\theta}}&=\hat{\mathbf{v}}_a a\pm\hat{\mathbf{h}}_a\sqrt{1-a^2}\\ \hat{\boldsymbol{\phi}}&=\pm\hat{\mathbf{v}}_a\sqrt{1-a^2}-\hat{\mathbf{h}}_a a\end{aligned} \tag{I-2.19}$$

where the $\pm$ is correlated between both vectors.

The definitions proposed by Ludwig focus on two linear components, $\hat{\mathbf{v}}$ and $\hat{\mathbf{h}}$. These represent the vertical and horizontal components respectively, defined in the frame of reference for the antenna pattern measurement. The typical frame of reference is the coordinate system and unit-vector definitions shown in Figure I-7.

Rotated Ludwig-3 unit vectors

Suppose it is desired to use a new linear reference, $\hat{\mathbf{v}}_\gamma$ and $\hat{\mathbf{h}}_\gamma$, which have been rotated with respect to the $\hat{\mathbf{v}}$ and $\hat{\mathbf{h}}$ of Figure I-7 by an angle γ. The rotation angle γ is defined so that a positive rotation moves $\hat{\mathbf{h}}$ toward $\hat{\mathbf{v}}$, as depicted in Figure I-7. This is a right-handed rotation with respect to the $\hat{\mathbf{z}}$ axis. For example, the equivalent of the Ludwig-3 for this new polarization is

$$\begin{aligned}\hat{\mathbf{v}}_{\gamma,3} &= \hat{\boldsymbol{\theta}}\sin(\phi-\gamma)+\hat{\boldsymbol{\phi}}\cos(\phi-\gamma)\\ \hat{\mathbf{h}}_{\gamma,3} &= \hat{\boldsymbol{\theta}}\cos(\phi-\gamma)-\hat{\boldsymbol{\phi}}\sin(\phi-\gamma)\end{aligned}. \tag{I-2.20}$$

Since (I-2.20) is simply (I-2.19) with $a=\sin(\phi-\gamma)$, the rotated Ludwig-3 vectors possess the involution property with respect to the spherical unit vectors $\hat{\boldsymbol{\theta}},\hat{\boldsymbol{\phi}}$. Evaluating the dot products $\hat{\mathbf{v}}_{\gamma,3}\cdot\hat{\mathbf{v}}_3$ and $\hat{\mathbf{h}}_{\gamma,3}\cdot\hat{\mathbf{h}}_3$ show that the angle between the rotated vectors and the nonrotated vectors is exactly the same, and equal to γ, everywhere over the sphere.

Roy-Shafai unit vectors

A "generalization" of the Ludwig-3 has been proposed by Roy and Shafai [18, 19], which is claimed to match the co-polarized and cross-polarized responses of the antenna better,

$$\begin{aligned}\hat{\mathbf{v}}_{RS} &= \hat{\boldsymbol{\theta}}\sin(\xi)+\hat{\boldsymbol{\phi}}\cos(\xi)\\ \hat{\mathbf{h}}_{RS} &= \hat{\boldsymbol{\theta}}\cos(\xi)-\hat{\boldsymbol{\phi}}\sin(\xi)\end{aligned}, \tag{I-2.21}$$

where

$$\xi=\tan^{-1}\left(\frac{\cos(\phi'-\phi)}{\cos\theta\sin(\phi'-\phi)}\right), \tag{I-2.22}$$

with the observation direction given by θ,ϕ, and ϕ' describing the direction of the ideal linearly polarized field: $\phi'=0$ corresponds to the electric field along the $\hat{\mathbf{x}}$ axis, and $\phi'=\pi/2$ corresponds to the electric field along the $\hat{\mathbf{y}}$ axis. This generalization is another of the class of involutory polarizations with respect to the spherical unit vectors $\hat{\boldsymbol{\theta}},\hat{\boldsymbol{\phi}}$. On the line $\theta=0$, if $\phi'=\gamma+\pi/2$, then $\xi=\phi-\gamma$, and the Roy-Shafai unit vectors are the same as the rotated Ludwig-3 unit vectors. Furthermore, when $\phi'=\pm\pi/2$, the Roy-Shafai unit vectors are parallel to the spherical unit vectors, $\hat{\boldsymbol{\theta}}',\hat{\boldsymbol{\phi}}'$, in a new coordinate system where $\hat{\mathbf{x}}'=\hat{\mathbf{y}}$, $\hat{\mathbf{y}}'=\hat{\mathbf{z}}$, and $\hat{\mathbf{z}}'=\hat{\mathbf{x}}$.

Comparison of linear polarization directions

As an aid to visualize the various sets of polarization basis vectors, they will be displayed on the surface of a sphere. The polarization unit-vector directions for the spherical, Ludwig 2, and Ludwig 3 unit-vector sets are plotted in Figure I-8. Similarly, the polarization directions for the pairs $\left(\hat{\mathbf{v}}_3,\hat{\mathbf{h}}_3\right)$, $\left(\hat{\mathbf{v}}_{\gamma,3},\hat{\mathbf{h}}_{\gamma,3}\right)$, and $\left(\hat{\mathbf{v}}_{RS},\hat{\mathbf{h}}_{RS}\right)$ are plotted in Figure I-9. The pair $\left(\hat{\mathbf{v}}_3,\hat{\mathbf{h}}_3\right)$ serves as a reference between the sets of plots, since it is repeated in each set.

Additional views of sets $\left(\hat{\theta},\hat{\phi}\right)$, $\left(\hat{\mathbf{v}}_2,\hat{\mathbf{h}}_2\right)$, and $\left(\hat{\mathbf{v}}_3,\hat{\mathbf{h}}_3\right)$ polarization unit vectors are illustrated in Figure I-10 and Figure I-11. In each row of Figure I-10, beginning with the top row, the observer is positioned on the positive $\hat{\mathbf{x}}$ axis, the positive $\hat{\mathbf{y}}$ axis, and the positive $\hat{\mathbf{z}}$, looking back toward the origin. In each row of Figure I-11, the observer is standing on the appropriate negative axis, looking toward the origin. Similarly, Figure I-12 and Figure I-13 present the same view, but for the polarization unit-vector pairs $\left(\hat{\mathbf{v}}_3,\hat{\mathbf{h}}_3\right)$, $\left(\hat{\mathbf{v}}_{\gamma,3},\hat{\mathbf{h}}_{\gamma,3}\right)$, and $\left(\hat{\mathbf{v}}_{RS},\hat{\mathbf{h}}_{RS}\right)$.

It is clear that the spherical unit vectors rotate about the $\hat{\mathbf{z}}$ axis as the angle ϕ varies, while the Ludwig unit vectors have nearly fixed directions near the poles associated with the $\hat{\mathbf{z}}$ axis. The ambiguity associated with the Ludwig-2 unit vectors at the points $\theta=\pi/2$, $\phi=\pi/2, 3\pi/2$ makes Ludwig's second definition problematic for describing antennas with significant radiation in those directions. The argument can be made that a similar problem occurs at points $\theta=0,\pi$ when the spherical unit vectors, $\hat{\theta}$ and $\hat{\phi}$, are used to represent the field. Indeed, this was the motivation behind Ludwig's definitions. The Ludwig-2 polarization can be useful for describing antennas that radiate primarily in the vicinity of the $\hat{\mathbf{z}}$ axis.

The Ludwig-3 polarization is well behaved in the $z>0$ hemisphere, but not in the lower hemisphere. Thus, the usefulness of this polarization will be greatest for linearly polarized antennas that radiate mostly into the $z>0$ hemisphere, and it is superior to the Ludwig-2 polarization when the antenna has significant radiation near the poles associated with the $\hat{\mathbf{y}}$ axis. It can be observed that the Ludwig-2 unit vectors are parallel to spherical unit vectors $\left(\hat{\theta}',\hat{\phi}'\right)$ defined in a coordinate system with the $\hat{\mathbf{z}}'$ axis aligned with the $\hat{\mathbf{y}}$ axis. Similarly, the Roy-Shafai unit vectors are parallel to spherical unit vectors defined in a coordinate system where the $\hat{\mathbf{z}}'$ axis is aligned with the $\hat{\mathbf{x}}$ axis. The Roy-Shafai unit vectors are much better behaved near the $-\hat{\mathbf{z}}$ than those of Ludwig-3, so they are useful when little radiation occurs near the $\pm\hat{\mathbf{x}}$ directions, but there is significant radiation in both the $\hat{\mathbf{z}}$ and $-\hat{\mathbf{z}}$ directions.

The Ludwig and Roy-Shafai polarization pairs are primarily useful only for describing linearly polarized antennas. The value of these polarization pairs is that by aligning the principal linear polarization of the antenna with one of the polarizations in a pair, two informative radiation patterns can be generated:

1) a pattern representing the best performance of the antenna in a link where the other antenna is an ideal linearly polarized antenna that is rotated as needed to match the principal polarization component of the first, and
2) a pattern representing the worst-case performance when the second antenna is rotated so its principal linear polarization is orthogonal to that of the first.

These two patterns can be designated the principal-polarization (or co-polarization) pattern and the cross-polarization pattern. The Ludwig polarization definitions can be quite useful for showing where the radiation from a linearly polarized antenna goes, but they can be cumbersome when calculating the link between a pair of antennas with arbitrary but known orientations. When the location and orientation of both antennas in a link are known, the representation using the components along the spherical unit vectors $\hat{\theta}$ and $\hat{\phi}$ may be the superior choice for many calculations.

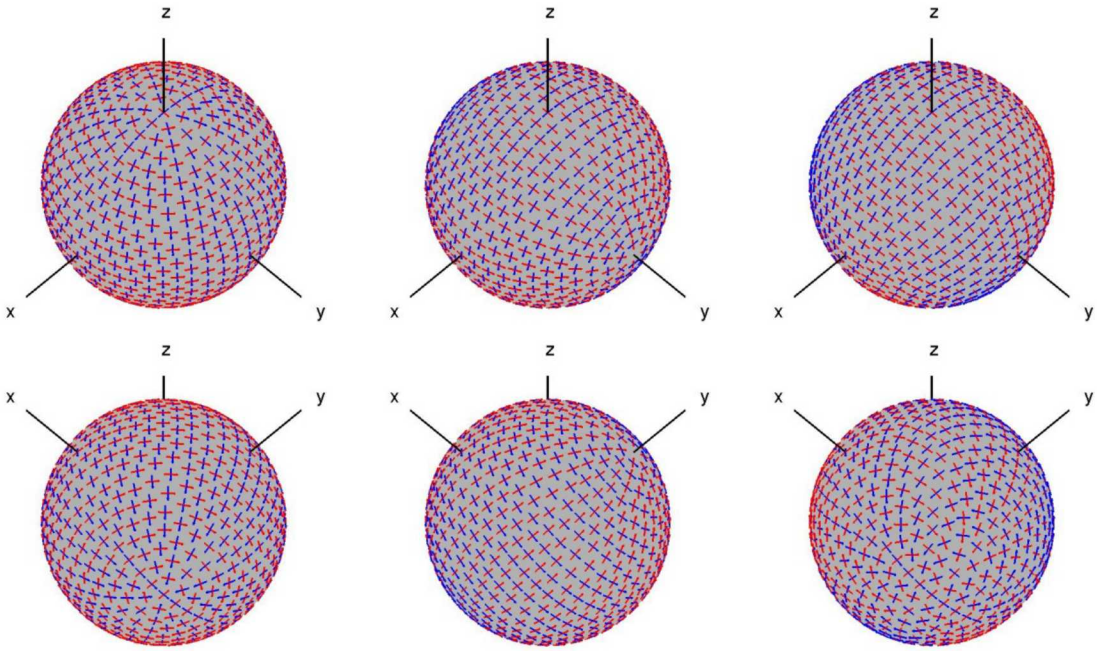

spherical unit vectors *Ludwig-2 unit vectors* *Ludwig-3 unit vectors*

Figure I-8 Unit vectors plotted on the surface of the sphere for standard spherical coordinate system (left), the Ludwig-2 polarizations (center), and the Ludwig-3 polarizations (right). The red arrows correspond to $\hat{\boldsymbol{\phi}}, \hat{\mathbf{v}}_2$, *or* $\hat{\mathbf{v}}_3$, *while the blue arrows correspond to* $\hat{\boldsymbol{\theta}}, \hat{\mathbf{h}}_2$, *or* $\hat{\mathbf{h}}_3$.

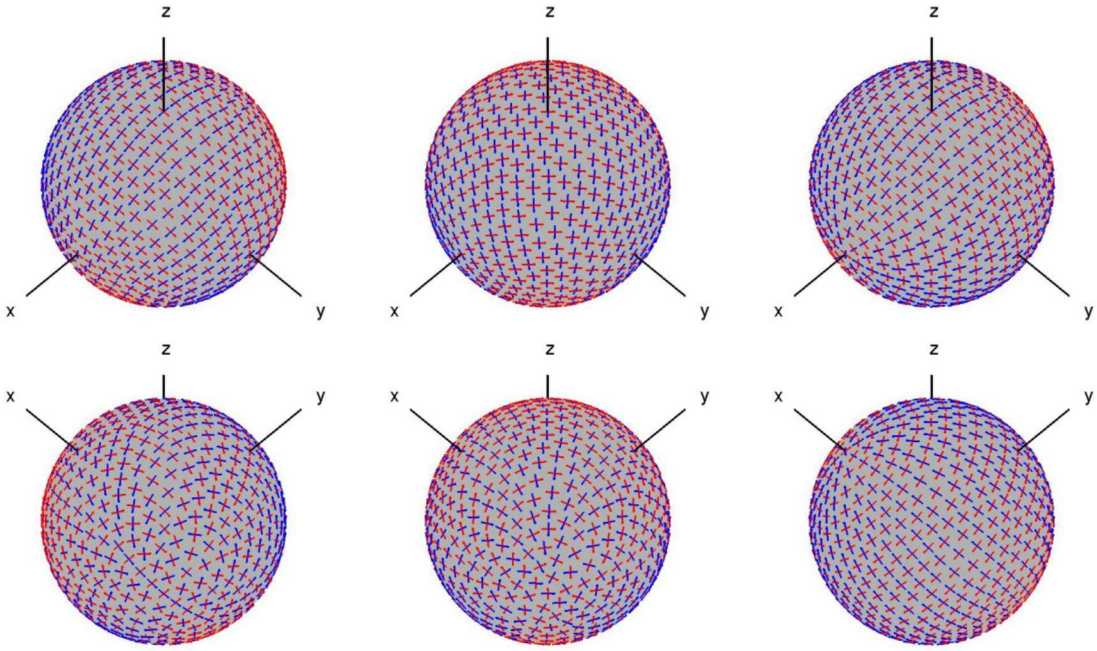

Ludwig-3 unit vectors *Ludwig-3 unit vectors rotated 45°* *Roy-Shafai unit vectors*

Figure I-9 Unit vectors plotted on the surface of the sphere for the Ludwig-3 polarizations, the Ludwig-3 polarizations after rotating 45° (center), and the Roy-Shafai polarizations (right). The red arrows correspond to $\hat{\mathbf{v}}_3, \hat{\mathbf{v}}_{\gamma,3}$, *or* $\hat{\mathbf{v}}_{RS}$, *while the blue arrows correspond to* $\hat{\mathbf{h}}_3, \hat{\mathbf{h}}_{\gamma,3}$, *or* $\hat{\mathbf{h}}_{RS}$.

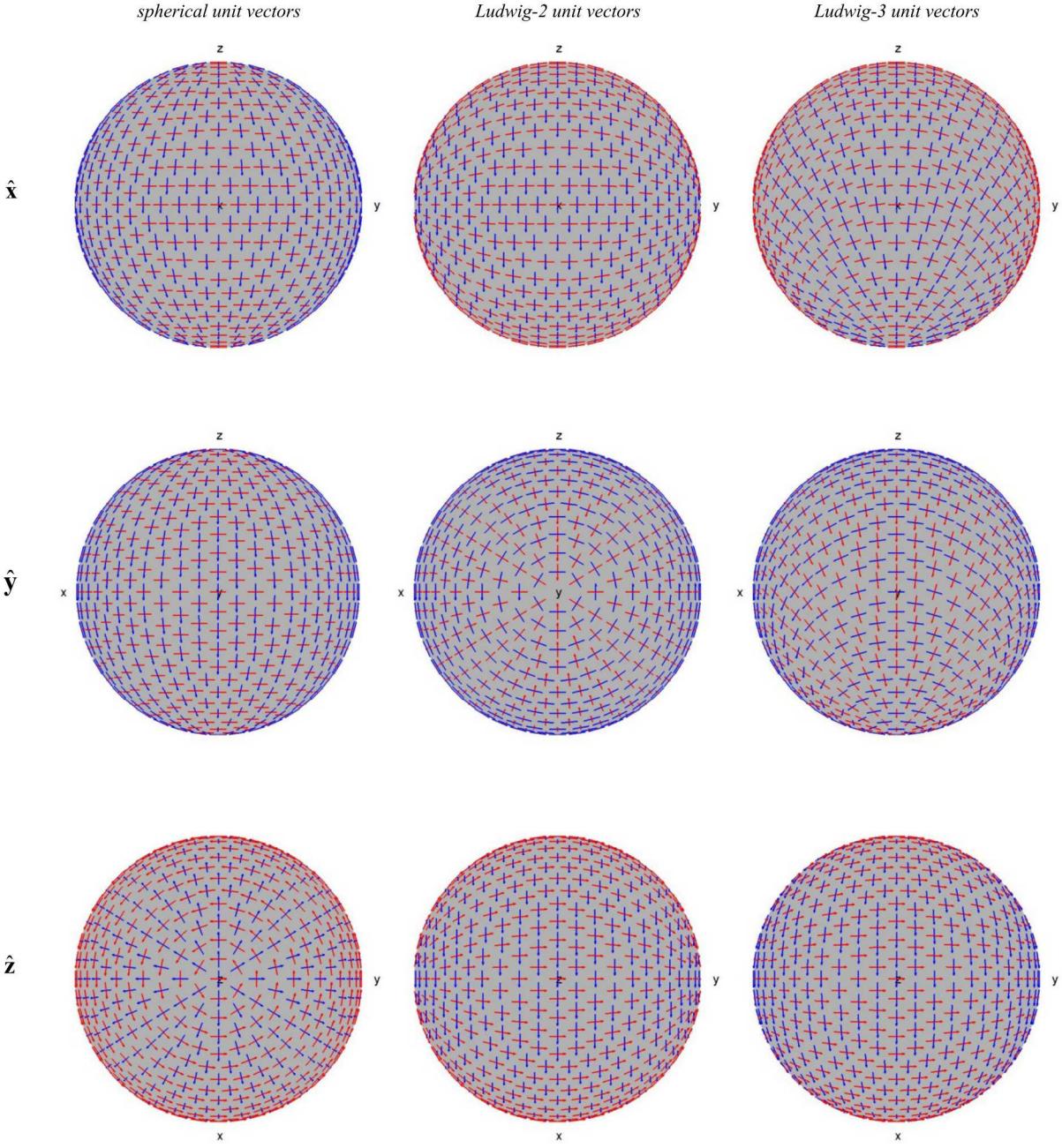

Figure I-10 Unit vectors plotted on the surface of the sphere for standard spherical coordinate system (left), the Ludwig-2 polarizations (center), and the Ludwig-3 polarizations (right). The red arrows correspond to $\hat{\boldsymbol{\phi}}, \hat{\mathbf{v}}_2$, *or* $\hat{\mathbf{v}}_3$, *while the blue arrows correspond to* $\hat{\boldsymbol{\theta}}, \hat{\mathbf{h}}_2$, *or* $\hat{\mathbf{h}}_3$, *as appropriate. The views are from a point on the* $\hat{\mathbf{x}}$ *axis (top),* $\hat{\mathbf{y}}$ *axis (middle), and* $\hat{\mathbf{z}}$ *axis (bottom).*

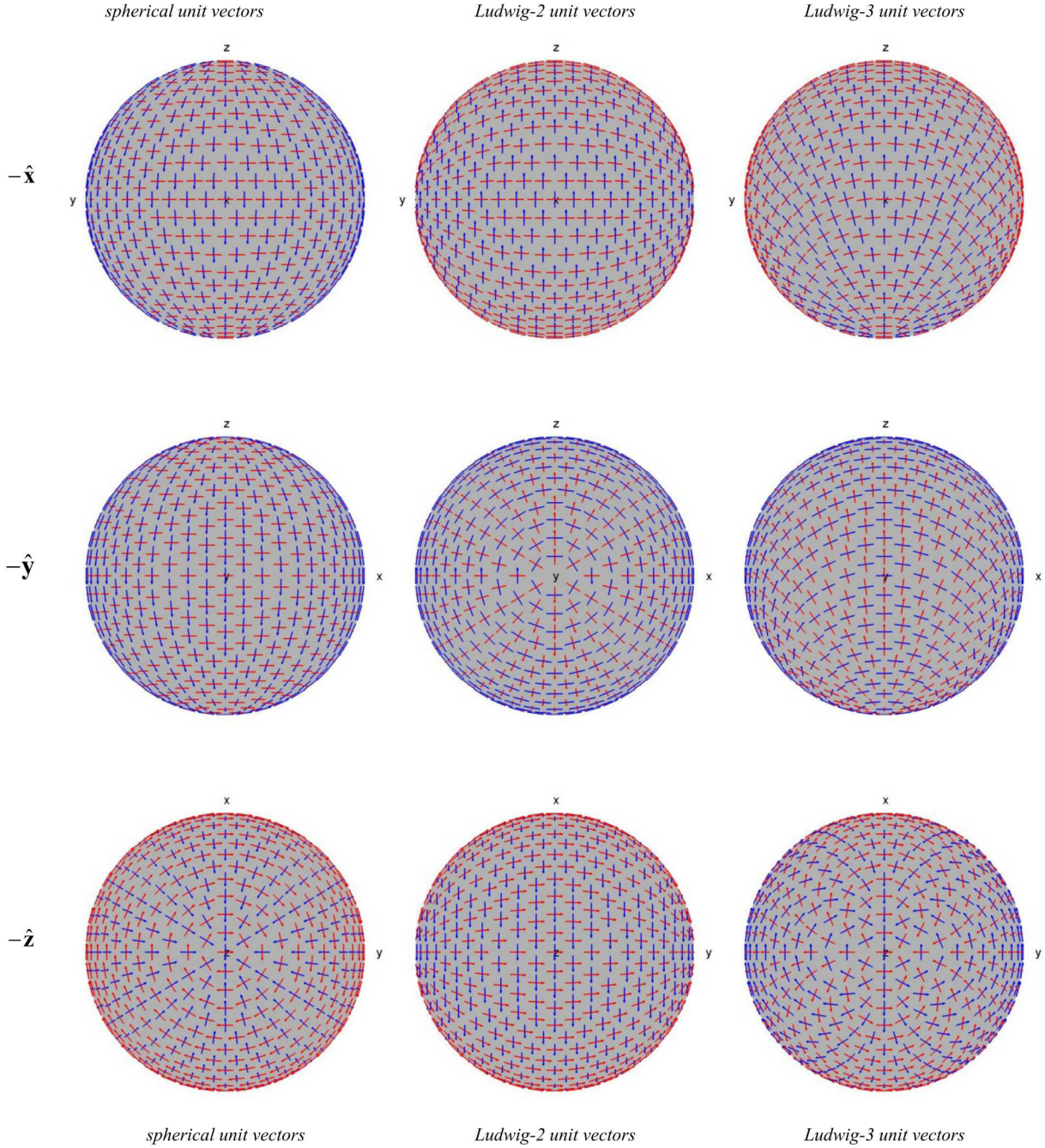

Figure I-11 Unit vectors plotted on the surface of the sphere for standard spherical coordinate system (left), the Ludwig-2 polarizations (center), and the Ludwig-3 polarizations (right). The red arrows correspond to $\hat{\boldsymbol{\phi}}, \hat{\mathbf{v}}_2$, *or* $\hat{\mathbf{v}}_3$, *while the blue arrows correspond to* $\hat{\boldsymbol{\theta}}, \hat{\mathbf{h}}_2$, *or* $\hat{\mathbf{h}}_3$, *as appropriate. The views are from a point on the* $-\hat{\mathbf{x}}$ *axis (top),* $-\hat{\mathbf{y}}$ *axis (middle), and* $-\hat{\mathbf{z}}$ *axis (bottom).*

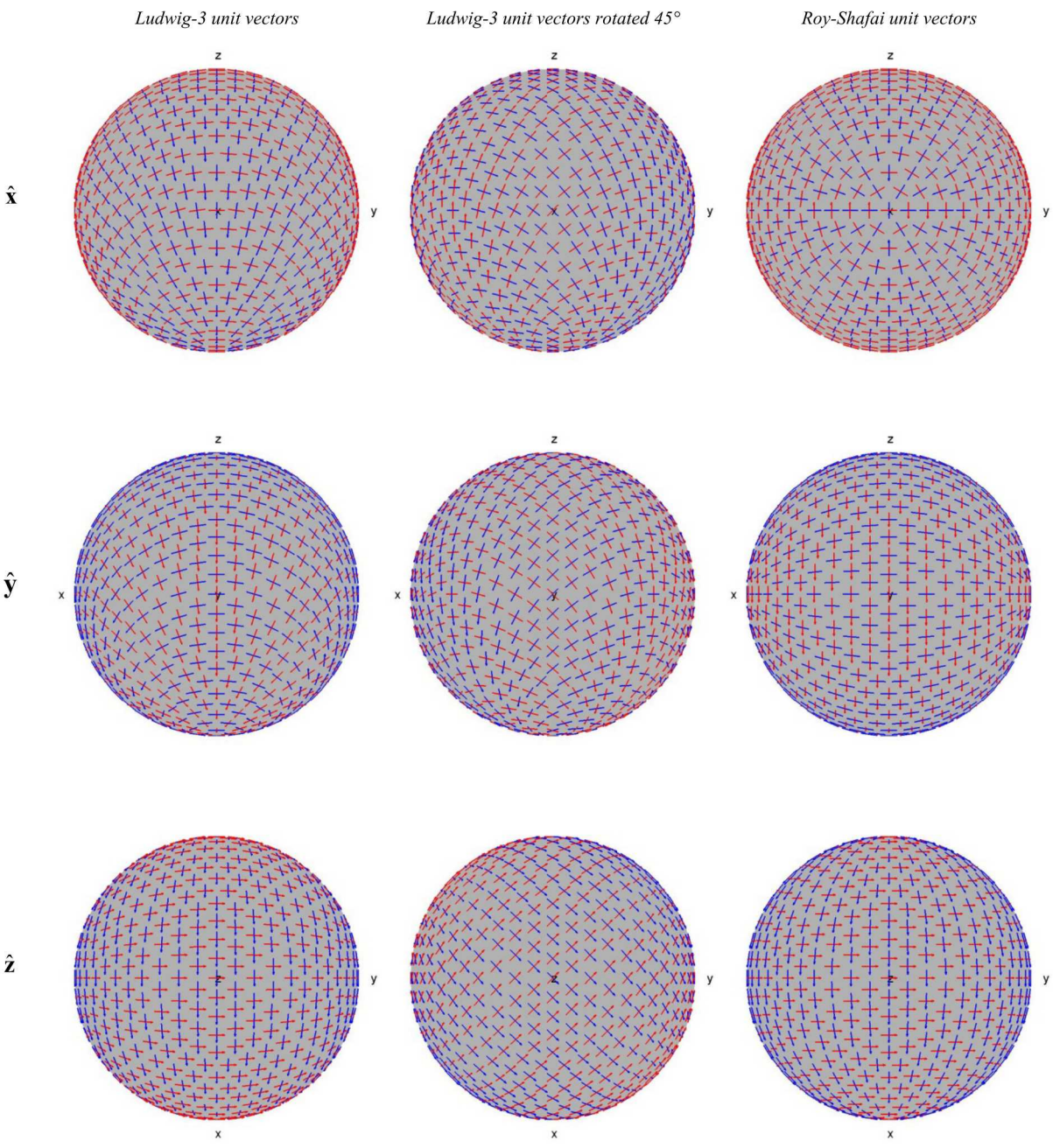

Figure I-12 Unit vectors plotted on the surface of the sphere for standard spherical coordinate system (left), the Ludwig-2 polarizations (center), and the Ludwig-3 polarizations (right). The red arrows correspond to $\hat{\mathbf{v}}_3$, $\hat{\mathbf{v}}_{\gamma,3}$, *or* $\hat{\mathbf{v}}_{RS}$, *while the blue arrows correspond to* $\hat{\mathbf{h}}_3$, $\hat{\mathbf{h}}_{\gamma,3}$, *or* $\hat{\mathbf{h}}_{RS}$, *as appropriate. The views are from a point on the* $\hat{\mathbf{x}}$ *axis (top),* $\hat{\mathbf{y}}$ *axis (middle), and* $\hat{\mathbf{z}}$ *axis (bottom).*

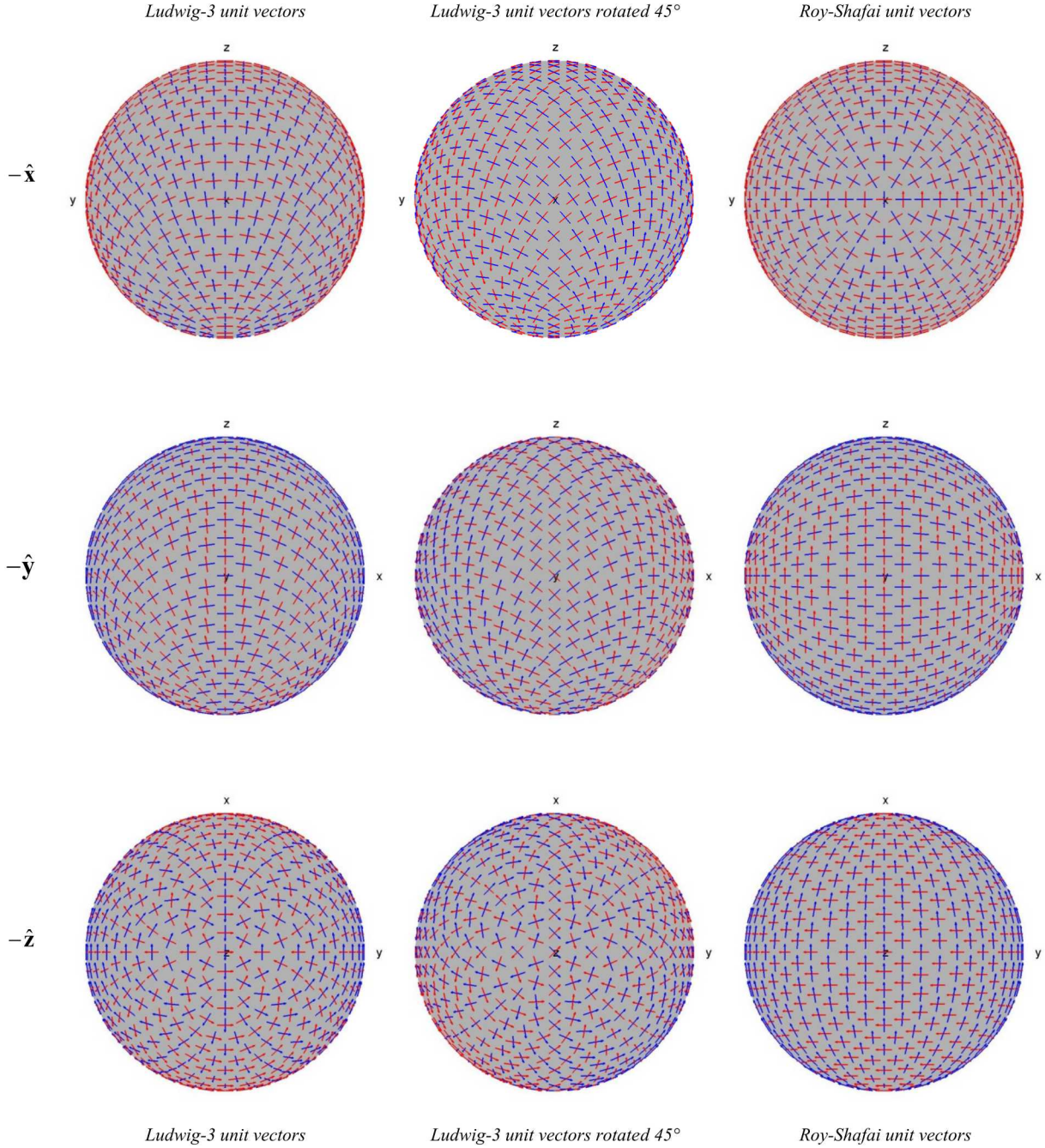

Figure I-13 Unit vectors plotted on the surface of the sphere for standard spherical coordinate system (left), the Ludwig-2 polarizations (center), and the Ludwig-3 polarizations (right). The red arrows correspond to $\hat{\mathbf{v}}_3$, $\hat{\mathbf{v}}_{\gamma,3}$, *or* $\hat{\mathbf{v}}_{RS}$, *while the blue arrows correspond to* $\hat{\mathbf{h}}_3$, $\hat{\mathbf{h}}_{\gamma,3}$, *or* $\hat{\mathbf{h}}_{RS}$, *as appropriate. The views are from a point on the* $-\hat{\mathbf{x}}$ *axis (top),* $-\hat{\mathbf{y}}$ *axis (middle), and* $-\hat{\mathbf{z}}$ *axis (bottom).*

Elliptical polarization

The polarization of the electromagnetic field, in the most general sense, is elliptical. That is, the electric-field vector rotates around the direction of propagation, and its tip traces an ellipse over the course of one cycle of the time-harmonic field. The ellipse can degenerate into a line, in which case the polarization is linear. Similarly, the ellipse can become a circle, in which case the polarization is called circular.

Because the general case is a rotating electric-field vector, it becomes necessary to define the direction of rotation. According to the *IEEE* [3, 4, 5], a right-handed field rotates clockwise when viewed looking the *direction of propagation*. When the thumb of the right hand is pointed in the direction of propagation, the fingers curl in the direction of the rotation of a right-handed field. A left-handed field rotates in the opposite direction. Although this is the definition that will be applied here, it should be recognized that this definition is not universal. For example, Stratton defines right-hand polarization with the electric-field vector rotating clockwise when the observer is looking toward the source (opposite the direction of propagation) [6] (see page 280); the same definition is used by Born and Wolf [1] (see page 29). The standard definition of the *IEEE* is in common usage in the antenna community, and is used in most standard texts on antennas, engineering electromagnetics, and radio-wave propagation. For example Harrington [7] , Weeks [8], Collin and Zucker [9], Kraus [10, 11], Elliot [12] , Stutzman and Thiele [13], Balanis [14, 15], and Ishimaru [16] all adhere to this convention. Most of the time in an engineering context, the *IEEE* definition is used, while in physics and optics, the opposite definition is most often used.

Circular polarization

Instead of using linear basis vectors to describe the field, it can be described with right-hand and left-hand rotating unit vectors,

$$\vec{\mathbf{E}} = E_{RHC}\hat{\mathbf{e}}_{RHC} + E_{LHC}\hat{\mathbf{e}}_{LHC}\,, \tag{I-3.1}$$

called right-hand circular (RHC) and left-hand circular (LHC) polarizations. For a phasor representation of the field, the coefficients $E_\theta, E_\phi, E_{RHC}, E_{LHC}$ are, in general, complex. The angle of each complex coefficient is called the phase of that component.

To reiterate, the *IEEE* standard designates right-hand polarization as the electric field rotating in a right-hand sense *with respect to the direction of propagation* [3]. Left-hand polarization is that which rotates in the opposite direction, in the left-hand sense with respect to the direction of propagation. Assuming time dependence of $e^{j\omega t}$ for the phasor fields, the right-hand circular unit vector is written

$$\hat{\mathbf{e}}_{RHC} = \frac{1}{\sqrt{2}}\left(\hat{\boldsymbol{\theta}} - j\hat{\boldsymbol{\phi}}\right). \tag{I-3.2}$$

The left-hand circular unit vector, which is orthogonal to (I-3.2) is

$$\hat{\mathbf{e}}_{LHC} = \frac{1}{\sqrt{2}}\left(\hat{\boldsymbol{\theta}} + j\hat{\boldsymbol{\phi}}\right). \tag{I-3.3}$$

The linear unit vectors can also be expressed in terms of the circular unit vectors

$$\hat{\boldsymbol{\theta}} = \frac{1}{\sqrt{2}}\left(\hat{\mathbf{e}}_{RHC} + \hat{\mathbf{e}}_{LHC}\right), \tag{I-3.4}$$

and

$$\hat{\boldsymbol{\phi}} = j\frac{1}{\sqrt{2}}\left(\hat{\mathbf{e}}_{RHC} - \hat{\mathbf{e}}_{LHC}\right). \tag{I-3.5}$$

Details of elliptical polarization

The most general polarimetric description of a particular wave is elliptical polarization, where the electric-field vector both rotates and changes length as it propagates, tracing an ellipse, as illustrated in Figure I-14. The simplest description of the ellipse is in the $\hat{\mathbf{u}}, \hat{\mathbf{v}}, \hat{\mathbf{r}}$ coordinate system where $\hat{\mathbf{r}}$ is the direction of propagation and $\hat{\mathbf{u}}, \hat{\mathbf{v}}$ are aligned with the semi-major and semi-minor axes of the ellipse. To illustrate the elliptical nature of the motion of the electric-field vector, the field can be written as the time function

$$\vec{\mathbf{E}}(t) = \hat{\mathbf{u}} E_a \cos\tau + \hat{\mathbf{v}} E_b \sin\tau \tag{I-3.6}$$

where $\tau = \omega t - kR$ is the parametric angle, evaluated at a distance R from the reference point. The unit vectors can be written as combinations of the spherical unit vectors as

$$\hat{\mathbf{u}} = \hat{\boldsymbol{\theta}} \cos\psi + \hat{\boldsymbol{\phi}} \sin\psi\,, \tag{I-3.7}$$

and

$$\hat{\mathbf{v}} = -\hat{\boldsymbol{\theta}} \sin\psi + \hat{\boldsymbol{\phi}} \cos\psi\,. \tag{I-3.8}$$

The tilt angle ψ is limited to the range

$$-\frac{\pi}{2} \le \psi \le \frac{\pi}{2}. \tag{I-3.9}$$

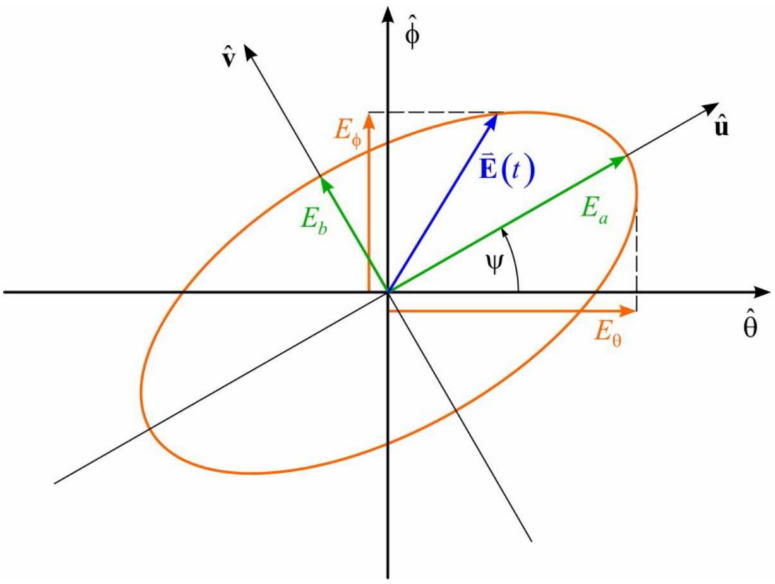

Figure I-14 General polarization ellipse, representing the most general description of a monochromatic, polarized electromagnetic wave.

The semi-major and semi-minor radii of the ellipse are E_a and E_b, respectively which are defined here so that $E_a > 0$, $E_b \ge 0$, and $E_a \ge E_b$. The polarization ellipse can be characterized by the axial ratio, defined by the *IEEE* to be the semi-major radius divided by the semi-minor radius,

$$AR = \pm\frac{E_a}{E_b}, \tag{I-3.10}$$

where the positive sign is used for *right-handed* rotation, and the negative sign is used for left-handed rotation [3, 5]. However, others define the sign of the axial ratio to be positive for left-hand rotation [14, 16]. Still others define the axial ratio as the semi-minor radius divided by the semi-major radius [20],

which has merit since the denominator will never be zero. However, using the *IEEE* definition, and since $E_a \geq E_b$, the axial ratio falls in the range $1 \leq |AR| \leq \infty$.

The field can be assigned a field strength, E_0, and an ellipticity angle, χ, such that

$$E_a = E_0 \cos\chi, \text{ and } E_b = E_0 \sin\chi, \tag{I-3.11}$$

so

$$\tan\chi = \pm\frac{E_b}{E_a}, \tag{I-3.12}$$

and

$$AR = \frac{1}{\tan\chi}. \tag{I-3.13}$$

Since $E_b \leq E_a$, the angle χ is restricted to

$$-\pi/4 \leq \chi \leq \pi/4. \tag{I-3.14}$$

The polarization ellipse can also be characterized by its eccentricity,

$$\varepsilon = \sqrt{1-\frac{E_b^2}{E_a^2}} = \sqrt{1-\tan^2\chi} < 1, \text{ or } \frac{E_b}{E_a} = \sqrt{1-\varepsilon^2}, \tag{I-3.15}$$

which leads to

$$\tan(2\chi) = \pm\frac{2E_bE_a}{\left(E_a^2 - E_b^2\right)} = \pm\frac{2\sqrt{1-\varepsilon^2}}{\varepsilon^2}. \tag{I-3.16}$$

Note that it is still assumed that $E_b \leq E_a$. However, by adding $\pm\pi/2$ to ψ, the semi-major and semi-minor axes can be interchanged in Figure I-14.

The field can also be described with basis vectors corresponding to the unit vectors $\hat{\theta}, \hat{\phi}$ of the spherical coordinate system, illustrated in Figure I-14, where the propagation direction $\hat{\mathbf{r}}$ is out of the page. In this case, the field is

$$\vec{\mathbf{E}}(t) = \hat{\theta}E_\theta \cos(\tau + \delta_\theta) + \hat{\phi}E_\phi \sin(\tau + \delta_\phi) \tag{I-3.17}$$

where δ_θ and δ_ϕ are the phase offsets necessary to ensure (I-3.17) describes the same field as described by (I-3.6). Of course phase is relative, so with the substitution $\tau' = \tau - \delta_\theta$, the same elliptical polarization could be described using only the phase difference, $\delta = \delta_\phi - \delta_\theta$, although the tip of the electric field vector would not be at the same point on the ellipse at the same value of τ. Equating (I-3.6) and (I-3.17) leads to

$$E_\theta = \sqrt{E_a^2\cos^2\psi + E_b^2\sin^2\psi}, \tag{I-3.18}$$

$$E_\phi = \sqrt{E_a^2\sin^2\psi + E_b^2\cos^2\psi}, \tag{I-3.19}$$

$$\tan\delta_\theta = \frac{E_b}{E_a}\tan\psi = \sqrt{1-\varepsilon^2}\tan\psi, \tag{I-3.20}$$

and

$$\tan\delta_\phi = \frac{E_a}{E_b}\tan\psi = \frac{\tan\psi}{\sqrt{1-\varepsilon^2}}. \tag{I-3.21}$$

As noted above, the same elliptical polarization (with slightly different phase) can be written

$$\vec{\mathbf{E}}(t') = \hat{\theta} E_\theta \cos\tau' + \hat{\phi} E_\phi \sin(\tau' + \delta), \tag{I-3.22}$$

where the $'$ indicates that the time/rotation variable is different to account for the phase difference ($t' \neq t$), and

$$\tan\delta = \frac{\left(E_a^2 - \mathrm{E}_b^2\right)}{2E_a E_b}\sin(2\psi) = \frac{\varepsilon^2}{2\sqrt{1-\varepsilon^2}}\sin(2\psi). \tag{I-3.23}$$

Since the phasor representation is often used for monochromatic fields, it is useful to write unit vectors representing orthogonal elliptical polarizations in the form of phasors. The phasor representation of (I-3.22) is

$$\begin{aligned}\vec{\mathbf{E}}'(t) &= \left(\hat{\theta} E_\theta - j\hat{\phi} E_\phi e^{j\delta}\right) e^{j\tau} \\ &= \sqrt{|E_a|^2 + |E_b|^2}\,\frac{1}{\sqrt{2-\varepsilon^2}}\left(\hat{\theta}\sqrt{1-\varepsilon^2\sin^2\psi} - j\hat{\phi}\sqrt{1-\varepsilon^2\cos^2\psi}\,e^{j\delta}\right)e^{j\tau}.\end{aligned} \tag{I-3.24}$$

Complex unit vectors for elliptical polarization are defined

$$\hat{\mathbf{e}}_{RHE}(\varepsilon,\psi) = \frac{1}{\sqrt{2-\varepsilon^2}}\left(\hat{\theta}\sqrt{1-\varepsilon^2\sin^2\psi} - j\hat{\phi}\sqrt{1-\varepsilon^2\cos^2\psi}\,e^{j\delta}\right), \tag{I-3.25}$$

and

$$\hat{\mathbf{e}}_{LHE}(\varepsilon,\psi) = \frac{1}{\sqrt{2-\varepsilon^2}}\left(\hat{\theta}\sqrt{1-\varepsilon^2\cos^2\psi} + j\hat{\phi}\sqrt{1-\varepsilon^2\sin^2\psi}\,e^{j\delta}\right), \tag{I-3.26}$$

where

$$\delta = \tan^{-1}\left(\frac{\varepsilon^2\sin(2\psi)}{2\sqrt{1-\varepsilon^2}}\right), \tag{I-3.27}$$

with

$$\sin\delta = \frac{\varepsilon^2\sin(2\psi)}{\sqrt{\varepsilon^4\sin^2(2\psi) + 4\left(1-\varepsilon^2\right)}} \text{ and } \cos\delta = \frac{2\sqrt{1-\varepsilon^2}}{\sqrt{\varepsilon^4\sin^2(2\psi) + 4\left(1-\varepsilon^2\right)}}. \tag{I-3.28}$$

The elliptical unit vectors can also be expressed in another form

$$\hat{\mathbf{e}}_{RHE}(\varepsilon,\psi) = \left(\hat{\theta}\cos\zeta - j\hat{\phi}\sin\zeta e^{j\delta}\right), \tag{I-3.29}$$

and

$$\hat{\mathbf{e}}_{LHE}(\varepsilon,\psi) = \left(\hat{\theta}\sin\zeta + j\hat{\phi}\cos\zeta e^{j\delta}\right), \tag{I-3.30}$$

where

$$\zeta(\varepsilon,\psi) = \tan^{-1}\left(\frac{\sqrt{1-\varepsilon^2\cos^2\psi}}{\sqrt{1-\varepsilon^2\sin^2\psi}}\right). \tag{I-3.31}$$

The value of ζ is related to the maximum amplitude in each of the pure $\hat{\theta}$ and $\hat{\phi}$ polarizations. If the eccentricity is known, then the tilt is obtained from

$$\psi = \cos^{-1}\left(\frac{1}{\varepsilon}\sqrt{\cos^2\zeta - \left(1-\varepsilon^2\right)\sin^2\zeta}\right). \tag{I-3.32}$$

When $\varepsilon = 0$, the tilt angle ψ is irrelevant, so that the elliptical polarizations become circular,

$$\hat{\mathbf{e}}_{RHE}\left(0,\psi\right)=\hat{\mathbf{e}}_{RHC} \tag{I-3.33}$$

and

$$\hat{\mathbf{e}}_{LHE}\left(0,\psi\right)=\hat{\mathbf{e}}_{LHC}\,. \tag{I-3.34}$$

Also, the linear polarizations are obtained when $\varepsilon\to 1$. However, care must be taken when evaluating (I-3.27) in the limit, to ensure that ε is approached from the correct side. Recalling the range for ψ as given by (I-3.9), and approaching the limit from $\varepsilon<1$, the limits are evaluated to yield

$$\lim_{\varepsilon\to 1}\left[\hat{\mathbf{e}}_{RHE}\left(\varepsilon,\psi\right)\right]=\hat{\theta}\cos\psi+\hat{\phi}\sin\psi\,, \tag{I-3.35}$$

and

$$\lim_{\varepsilon\to 1}\left[\hat{\mathbf{e}}_{LHE}\left(\varepsilon,\psi\right)\right]=\hat{\theta}\sin\psi+\hat{\phi}\cos\psi\,. \tag{I-3.36}$$

References

[1] Max Born and Emil Wolf, *Principles of Optics, 7th edition,* Cambridge University Press, Cambridge, 1999.

[2] Petr Beckmann, *The Depolarization of Electromagnetic Waves*, The Golem Press, Boulder, 1968.

[3] *IEEE Standard Test Procedures for Antennas*, ANSI/IEEE Std 149-1979, The Institute of Electrical and Electronics Engineers, Inc., New York, 1979.

[4] *IEEE Standard Definitions of Terms for Radio Wave Propagation*, IEEE Std 211-1997, The Institute of Electrical and Electronics Engineers, Inc., New York, 1998.

[5] *IEEE Standard Definitions of Terms for Antennas*, IEEE Std 145-1993, The Institute of Electrical and Electronics Engineers, Inc., New York, 1993.

[6] Julius Adams Stratton, *Electromagnetic Theory*, McGraw-Hill Book Company, New York, 1941.

[7] Roger F. Harrington, *Time-harmonic Electromagnetic Fields*, McGraw-Hill Book Co., New York, 1961, reissued 1987.

[8] W. L. Weeks, *Electromagnetic Theory for Engineering Applications*, John Wiley & Sons, Inc., New York, 1964.

[9] Robert E. Collin and Francis J. Zucker, *Antenna Theory Part 1*, McGraw-Hill Book Company, New York, 1969.

[10] John D. Kraus, *Electromagnetics, third edition*, McGraw-Hill Book Co., New York, 1984.

[11] John D. Kraus, *Antennas, second edition*, McGraw-Hill Book Co., New York, 1988.

[12] Robert S. Elliot, *Antenna Theory and Design*, Prentice-Hall, Inc., Englewood Cliffs, 1981.

[13] Warren L. Stutzman, Gary A. Thiele, *Antenna Theory and Design*, John Wiley & Sons, New York, 1981.

[14] Constantine A. Balanis, *Advanced Engineering Electromagnetics*, John Wiley & Sons, Inc., New York, 1989.

[15] Constantine A. Balanis, *Antenna Theory: Analysis and Design, second edition*, John Wiley & Sons, Inc., New York, 1997.

[16] Akira Ishimaru, *Wave Propagation and Scattering in Random Media*, New York, IEEE Press and Oxford University Press, 1997. (Originally published: New York, Academic Press, 1978.)

[17] Arthur C. Ludwig, "The Definition of Cross Polarization", *IEEE Transactions on Antennas and Propagation*, Vol. 21, No. 1, January, 1973, pp 116-119.

[18] J. E. Roy and L. Shafai, "Generalization of the Ludwig-3 Definition for Linear Copolarization and Cross Polarization", *IEEE Transactions on Antennas and Propagation*, Vol. 49, No. 6, June 2001, pp 1006-1010.

[19] J. E. Roy and L. Shafai, Corrections to "Generalization of the Ludwig-3 Definition for Linear Copolarization and Cross Polarization", *IEEE Transactions on Antennas and Propagation*, Vol. 52, No. 2, Feb. 2004, pp 638-639.

[20] Georges A. Deschamps and P. Edward Mast, "Poincaré Sphere Representation of Partially Polarized Fields", *IEEE Transactions on Antennas and Propagation*, Vol. 21, No. 4, July. 1973, pp 474-478.

Appendix II – Scale-invariant solutions of Maxwell's equations

The application of dimensional and frequency scaling is well known in the field of electromagnetics. Nevertheless, it is useful to re-examine and understand the behavior of solutions to Maxwell's equations when spatial dimensions are scaled. Since Maxwell's equations are not scale-invariant in the most general sense, the conditions for which scale-invariant solutions exist will be examined below.

The vector fields will be described by the time-harmonic phasor representation with time dependence given by $e^{j\omega t}$. The radian frequency is $\omega = 2\pi f$, f is the temporal frequency (measured in hertz), and t is time (measured in seconds). The time-harmonic electromagnetic field will satisfy the phasor form of Maxwell's differential equations:

$$\nabla \times \vec{\mathbf{E}} = -j\omega \vec{\mathbf{B}}, \tag{II-1.1}$$

$$\nabla \times \vec{\mathbf{H}} = j\omega \vec{\mathbf{D}} + \vec{\mathbf{J}}, \tag{II-1.2}$$

$$\nabla \cdot \vec{\mathbf{B}} = \mathbf{0}, \tag{II-1.3}$$

and

$$\nabla \cdot \vec{\mathbf{D}} = \rho, \tag{II-1.4}$$

where $\vec{\mathbf{E}}$ is the electric field intensity (V/m), $\vec{\mathbf{H}}$ is the magnetic field intensity (A/m), $\vec{\mathbf{D}}$ is the electric flux density (A s/m^2), $\vec{\mathbf{B}}$ is the magnetic flux density (V s/m^2), $\vec{\mathbf{J}}$ is the electric current density (A/m^2), and ρ is the electric charge density (A s/m^3). Following the common practice, the time dependence will be suppressed, and the field quantities will be considered to be functions of the spatial position $\vec{\mathbf{r}} = x\hat{\mathbf{x}} + y\hat{\mathbf{y}} + z\hat{\mathbf{z}}$ and radian frequency ω.

The field flux densities are functions of the associated field intensities. In what follows, it will be assumed that the relationship is linear, so the following constitutive relations will be applied,

$$\vec{\mathbf{D}} = \bar{\bar{\varepsilon}} \cdot \vec{\mathbf{E}}, \tag{II-1.5}$$

and

$$\vec{\mathbf{B}} = \bar{\bar{\mu}} \cdot \vec{\mathbf{H}}, \tag{II-1.6}$$

where $\bar{\bar{\varepsilon}}$ is the electric permittivity and $\bar{\bar{\mu}}$ is the magnetic permeability of the material in which the field exist. In the source-free region, the charge density in (II-1.4) is zero, and with no source currents, the current density is related to the electric field intensity

$$\vec{\mathbf{J}} = \bar{\bar{\sigma}} \cdot \vec{\mathbf{E}}, \tag{II-1.7}$$

where $\bar{\bar{\sigma}}$ is the electric conductivity. The permittivity, permeability, and conductivity are written as dyadic quantities to accommodate anisotropic material, but in the vast majority of practical applications, the materials are isotropic. In this case, each dyadic can be replaced with a scalar quantity.

Applying the constitutive relations, the electromagnetic field in the source-free region must satisfy

$$\nabla \times \vec{\mathbf{E}} = -j\omega \bar{\bar{\mu}} \cdot \vec{\mathbf{H}} \tag{II-1.8}$$

$$\nabla \times \vec{\mathbf{H}} = \left(j\omega \bar{\bar{\varepsilon}} + \bar{\bar{\sigma}} \right) \cdot \vec{\mathbf{E}} \tag{II-1.9}$$

$$\nabla \cdot \bar{\bar{\mu}} \cdot \vec{\mathbf{H}} = \mathbf{0} \tag{II-1.10}$$

and

$$\nabla \cdot \bar{\bar{\varepsilon}} \cdot \vec{\mathbf{E}} = 0. \tag{II-1.11}$$

Now, consider scaling the coordinates so that $\vec{\mathbf{r}}' = \vec{\mathbf{r}}/\alpha$, where $\alpha \neq 0$. With respect to the primed coordinates, the operator ∇' is

$$\nabla' = \hat{\mathbf{x}}\frac{\partial}{\partial x'} + \hat{\mathbf{y}}\frac{\partial}{\partial y'} + \hat{\mathbf{z}}\frac{\partial}{\partial z'} = \hat{\mathbf{x}}\frac{dx}{dx'}\frac{\partial}{\partial x} + \hat{\mathbf{y}}\frac{dy}{dy'}\frac{\partial}{\partial y} + \hat{\mathbf{z}}\frac{dz}{dz'}\frac{\partial}{\partial z} = \alpha\nabla . \tag{II-1.12}$$

An electromagnetic field $\vec{\mathbf{E}}', \vec{\mathbf{H}}'$ existing in the source-free region must satisfy the following equations in the primed coordinate system,

$$\nabla' \times \vec{\mathbf{E}}' = -j\omega' \bar{\bar{\mu}}' \cdot \vec{\mathbf{H}}' \tag{II-1.13}$$

$$\nabla' \times \vec{\mathbf{H}}' = \left(j\omega' \bar{\bar{\varepsilon}}' + \bar{\bar{\sigma}}' \right) \cdot \vec{\mathbf{E}}' \tag{II-1.14}$$

$$\nabla' \cdot \bar{\bar{\mu}}' \cdot \vec{\mathbf{H}}' = \mathbf{0} \tag{II-1.15}$$

and

$$\nabla' \cdot \bar{\bar{\varepsilon}}' \cdot \vec{\mathbf{E}}' = 0 . \tag{II-1.16}$$

Rewriting these equations with respect to the unscaled coordinate system gives,

$$\alpha\nabla \times \vec{\mathbf{E}}' = -j\omega' \bar{\bar{\mu}}' \cdot \vec{\mathbf{H}}' \tag{II-1.17}$$

$$\alpha\nabla \times \vec{\mathbf{H}}' = \left(j\omega' \bar{\bar{\varepsilon}}' + \bar{\bar{\sigma}}' \right) \cdot \vec{\mathbf{E}}' \tag{II-1.18}$$

$$\alpha\nabla \cdot \bar{\bar{\mu}}' \cdot \vec{\mathbf{H}}' = \mathbf{0} \tag{II-1.19}$$

and

$$\alpha\nabla \cdot \bar{\bar{\varepsilon}}' \cdot \vec{\mathbf{E}}' = 0 . \tag{II-1.20}$$

When the following substitutions are made, then (II-1.17) through (II-1.20) are indistinguishable from (II-1.13) through (II-1.16)

$$\omega' = \alpha\omega, \tag{II-1.21}$$

$$\bar{\bar{\varepsilon}}' = \bar{\bar{\varepsilon}} , \tag{II-1.22}$$

$$\bar{\bar{\mu}}' = \bar{\bar{\mu}} , \tag{II-1.23}$$

and

$$\bar{\bar{\sigma}}' = \alpha\bar{\bar{\sigma}} . \tag{II-1.24}$$

In this case, when the same boundary conditions are applied, the solution for $\vec{\mathbf{E}}, \vec{\mathbf{H}}$ from (II-1.13) through (II-1.16) is identical to the solution for $\vec{\mathbf{E}}', \vec{\mathbf{H}}'$ from (II-1.17) through (II-1.20). When (II-1.21) through (II-1.24) are true, then Maxwell's equations are scalar-invariant.

Note that it is not necessary that the medium be isotropic since the conclusion is the same whether the permittivity, permeability, and conductivity are dyadic or scalar quantities. It is also not necessary that the medium be homogeneous, as long as the inhomogeneity follows the scaling $\vec{\mathbf{r}}' = \vec{\mathbf{r}}/\alpha$. For example, if the inhomogeneity for $\vec{\mathbf{E}}, \vec{\mathbf{H}}$ is in the form of a stack of homogeneous layers of thickness d_i, then scale invariance requires that $d_i' = d_i/\alpha$ for $\vec{\mathbf{E}}', \vec{\mathbf{H}}'$, while $\bar{\bar{\varepsilon}}_i' = \bar{\bar{\varepsilon}}_i$, $\bar{\bar{\mu}}_i' = \bar{\bar{\mu}}_i$, and $\bar{\bar{\sigma}}_i' = \alpha\bar{\bar{\sigma}}_i$.

The practical result is that when $\bar{\bar{\sigma}} = 0$ and the permittivity and permeability remain unchanged, the solution to Maxwell's equations in the source-free region is the same for any scale such that $f' = \alpha f$ when the dimensions are scaled by $1/\alpha$.

When the conductivity is not zero, then scalar invariance requires that the conductivity be appropriately scaled in addition to scaling the frequency. However, when the conductivity is sufficiently large, the field is usually not computed inside the conductor. Instead, the conductor is treated as imposing boundary conditions on the solution for the electromagnetic field in the non-conducting region. In general, unless the boundary conditions are appropriately scaled, the solution will not be strictly scale-invariant, but in the limit as conductivity becomes infinite, the solution will still be scale-invariant. Thus, when the

conductivity is large enough for the boundary to be considered a perfect electric conductor, the solution will be scale-invariant. Since this is the case for most metals, scale invariance is available for many practical problems.

Scaling the frequency is not the only option available to achieve scale-invariant solutions to Maxwell's equations. The fundamental requirement to make a solution invariant to spatial scale $\vec{\mathbf{r}}' = \vec{\mathbf{r}}/\alpha$ is to require

$$\omega' \bar{\bar{\boldsymbol{\varepsilon}}}' = \alpha\omega \bar{\bar{\boldsymbol{\varepsilon}}}, \tag{II-1.25}$$

$$\omega' \bar{\bar{\boldsymbol{\mu}}}' = \alpha\omega \bar{\bar{\boldsymbol{\mu}}}, \tag{II-1.26}$$

and

$$\bar{\bar{\boldsymbol{\sigma}}}' = \alpha \bar{\bar{\boldsymbol{\sigma}}}. \tag{II-1.27}$$

For some situations, the electric permittivity and magnetic permeability can be scaled instead of the frequency, or in combination with the frequency, as long as the products satisfy (II-1.25) and (II-1.26). As a practical matter, it is usually too difficult to find materials with appropriately scaled permittivity, permeability, and conductivity to make this path to scale invariance practical.

Distribution

		John Fanelle (electronic copy) General Atomics ASI, RSG 16761 Via Del Campo Ct San Diego, CA 92127
1	MS 0519	Steven Castillo, 05346
1	MS 0519	Roger Derek West, 05346
1	MS 0519	Judith A. Ruffner, 05349
1	MS 0519	Armin W. Doerry, 05349
1	MS0519	Laura M. Klein, 05349
1	MS0519	Douglas L. Bickel, 05344
1	MS0519	Ann M. Raynal, 05344
1	MS 0532	Bryan L. Burns, 05300
1	MS 0532	William H. Hensley, Jr., 05344
1	MS 0533	Susan Gardner, 05342
1	MS 0533	Robert Riley, 05342
1	MS 0533	Kurt W. Sorensen, 05345
1	MS 0533	Steven E. Allen, 05345
1	MS 0533	Karen Coperich Branch, 05345
5	MS 0533	Billy C. Brock, 05345
1	MS 0533	Dale F. Dubbert, 05345
1	MS 0533	Travis W. Eubanks, 05345
1	MS 0533	Gary K. Froehlich, 05345
1	MS 0533	Hung (Jacques) Loui, 05345
1	MS 0533	Jacob J. McDonald, 05345
1	MS 0533	Ward E. Patitz, 05345
1	MS 0533	Bernd H. Strassner II, 05345
1	MS 0899	Technical Library, 9536 (electronic copy)


Sandia National Laboratories